Dynamic characteristics and crack evolution laws of coal and rock under split Hopkinson pressure bar impact loading

OPEN ACCESS
IOP Publishing
Measurement Science and Technology
Meas. Sci. Technol. **34** (2023) 075601 (25pp)
https://doi.org/10.1088/1361-6501/acca3b

Dynamic characteristics and crack evolution laws of coal and rock under split Hopkinson pressure bar impact loading

Xiaoyuan Sun[1,2], **Tingxu Jin**[1,*], **Jihui Li**[1], **Jianlin Xie**[1], **Chuantian Li**[1,2] and **Xiaoxia Li**[1,2]

[1] College of Safety and Emergency Management Engineering, Taiyuan University of Science and Technology, Taiyuan 030024, People's Republic of China
[2] Intelligent Monitoring and Control of Coal Mine Dust Key Laboratory of Shanxi Province, Taiyuan University of Science and Technology, Taiyuan 030024, People's Republic of China

E-mail: jintingxu1997@163.com

Received 6 January 2023, revised 30 March 2023
Accepted for publication 4 April 2023
Published 18 April 2023

Abstract

The dynamic mechanical properties and crack evolution characteristics of coal and rock during split Hopkinson pressure bar (SHPB) impact failure are important contents for analysis. In previous studies, the coal and rock specimens used have usually been independent and not closely correlated. In addition, quantitative characterization and analysis methods for coal and rock cracks are immature, and more information has not been fully revealed. The aims of this paper are to comprehensively explore both the dynamic mechanical properties and crack evolution characteristics of coal and rock during impact failure. First, experimental specimens are prepared from coal seam, direct roof rock strata and direct floor rock strata in the same area to highlight the correlations between test pieces. Second, a dynamic strain gauge and high-speed (HS) camera are adopted to reflect the stress wave signal and crack evolution. Then, based on digital image correlation (DIC) technology and the mass screening method, the evolution laws of surface cracks during crushing and the distribution characteristics of sample fragments after crushing are studied from the perspective of fractal, and finally compared with those of the simulation analysis. The results are as follows. (1) The coal and rock samples from the same area have both consistency and differences. The dynamic mechanical properties of coal and rock are affected by the impact velocity and the physical properties of the specimen. Higher impact speeds and densities lead to the more obvious brittleness of the specimen when destroyed. Conversely, the sample shows more plasticity and ductile yield. (2) The self-similarity is significantly manifested in the evolution of surface cracks during impact and the distribution characteristics of fragments after impact. The box dimension and quality screening dimension are applicable to quantitatively characterize the evolution process and results of coal and rock fractures. (3) The simulation results based on the Holmquist–Johnson–Cook (HJC) and Riedel–Hiermaier–Thoma (RHT) constitutive

* Author to whom any correspondence should be addressed.

models agree well with the experimental results, and the RHT constitutive model is more consistent. This study may contribute to a more comprehensive understanding of the dynamic characteristics and crack evolution laws of coal and rock under impact loading and provide references for further research and discussion.

Keywords: coal and rock masses, impact failure, dynamic mechanical properties, crack propagation, box dimension, crushing form

(Some figures may appear in colour only in the online journal)

1. Introduction

To date, an increasing number of mines are entering the state of deep mining [1]. Unlike shallow mining, deep coal and rock masses always exist in the special mechanical environment of three highs and one disturbance, i.e. high ground stress, high ground temperature, high karst water pressure and mining disturbance [2], resulting in a more complex mechanism. Mining disturbance mainly refers to blasting, crosscut coal uncovering, rapid mining and other production operations [3], with a relatively high strain rate, which is more likely to cause rapid changes in stress distribution and transient instability of coal and rock structure [4]. Statistics show that 96.5% [5] of outburst accidents and 93.3% [6] of rockburst are caused by external mining disturbances. More seriously, with the extension of the mining level, the consequences of coal and rock dynamic disasters induced by mining disturbance are becoming increasingly serious.

Studies on material failure and instability in the range of high strain rates (10^1–10^4) usually adopt the split Hopkinson pressure bar (SHPB) device [7]. By taking the dynamic compression of coal and rock as an example, the International Society for Rock Mechanics (ISRM) has proposed dynamic test methods of uniaxial compression [8] and triaxial compression [9]. Many scholars have made targeted improvements to SHPBs based on their needs. Li *et al* [10] and Gong *et al* [11] developed active confining pressure and axial pressure devices based on a conventional SHPB device and realized dynamic and static combined loading in a preliminary sense. Yin *et al* [12] added a temperature control device to SHPB and then analyzed the dynamic mechanical properties of rock under the coupling of temperature and pressure. However, in the above devices, the most commonly used device is still the uniaxial compression SHPB system, especially in the experiment of observing the crack evolution law during the impact compression failure of coal and rock.

Quantitative characterizations of the dynamic mechanics and fracture processes of coal and rock during SHPB impact failure are critical for evaluating the stability and failure processes of the system and are challenging subjects. Although traditional contact measurement technologies, such as strain gauges, characterize the dynamic mechanical properties of coal and rock through the stress−strain rate curve, they are still indirect reflection methods. This method cannot provide intuitive and sufficient information to fully reflect the evolution of cracks, nor is it conducive to an effective understanding of the failure mechanisms of coal and rock [7]. In this case, many optical testing technologies, such as laser measurement [13], molar technology [14], photoelectric technology [15], holographic interferometry [16], caustics [17], x-ray micro CT [18] and infrared thermal imaging technology [19], are applied to the study of coal and rock impact processes. With the introduction and development of high-speed (HS) photography [20] and digital image correlation (DIC) technology [21], HS–DIC technology, as a high-speed, high-resolution, noncontact and full-field observation technology, has been widely used in the field of coal and rock impact dynamics.

HS photos provide a synchronous relationship between crack initiation time and stress history [7], while DIC is an optical method for addressing the image differences before and after deformation [22]. For crack images of coal and rock, scholars have adopted different in-depth processing methods. Zhang and Zhao [23] integrated a dynamic stress−strain curve, dynamic horizontal strain fields and a normalized dynamic compressive strength function to verify the effectiveness of HS–DIC technology in rock crack analysis during uniaxial impact. Gao *et al* [22] applied HS–DIC technology to fracture measurements in notched semi-circular bend (NSCB) tests of rocks and extracted the crack tip positions and dynamic stress intensity factors. Ai *et al* [24, 25] used HS–DIC technology to study the crack propagation of coal and rock under the impact of SHPB. Germanovich *et al* [26], Dyskin *et al* [27], Lu *et al* [28], Fu *et al* [29], Li *et al* [30] and Zhang *et al* [31] discussed the influences of preset defects on rock crack growth with the help of DIC technology. Furthermore, to overcome the heterogeneous and opaque features of coal and rock, HS–DIC has been preliminarily applied in the crack failure of 3D printing samples [32–36]. However, although the above achievements provide some methods for analyzing cracks using HS–DIC technology, the accuracy and quantitative characterization of surface crack parameters still need to be improved. In this case, it is particularly necessary to use fractal theory to study the surface cracks of heterogeneous materials, such as coal and rock [37]. Li *et al* [38] and Ma *et al* [39] carried out fractal investigations on the surface crack evolution characteristics of coal and rock failure and achieved preliminary quantitative results.

Considering that the coal and rock samples prepared in the SHPB impact tests are mostly cylinders, it is difficult to accurately measure the circumferential deformation field and crack field under impact compression with one camera [23]. In addition, crack propagation in the specimen cannot be observed,

which greatly limits the application of HS–DIC. Therefore, many scholars adopt the mass screening method for analyzing the fragments of coal and rock after impact damage. Hou *et al* [40] carried out screening tests on slate, sandstone and granite fragments after SHPB impact and discussed the impact load and rock characteristics on the final results. Li *et al* [41] used the SHPB device to conduct impact tests on artificially prepared coal, rock and combined bodies and studied the mass fractal dimension of the fragments using the screening method.

We must emphasize that HS–DIC technology effectively characterizes the surface progressive fracture processes of coal and rock during impact, and the mass screening rule focuses on the distribution characteristics of fragments after impact. Both are closely related to fractal theory and have a temporal inheritance relationship. The unification of the two is helpful for comprehensively reflecting the dynamic characteristics and failure processes of coal and rock under impact conditions. To date, there are few studies on the comprehensive applications of surface crack and fragment characteristics to evaluate the impact damage degrees of coal and rock. In addition, as typical heterogeneous and anisotropic media, coal and rock specimens under high-velocity impact often show typical discontinuity and nonlinearity in the failure process [42]. Relative to the laboratory test, numerical simulation reveals the overall process and internal mechanism of sample failure from the detail level, which is crucial to the study of coal and rock impact [43]. Currently, common numerical methods including finite element method (FEM) [44], extended finite element method (XFEM) [45], numerical manifold method (NMM)[46], and phase-field method [47–49], are employed to simulate crack growth and failure. Notably, both the FEM and the phase-field method are simulation methods for crack propagation under the finite element framework, and have wide applications in the simulation of brittle materials such as rock [50, 51], coal [52, 53] and concrete [54–56].

In this paper, coal and rock samples obtained at the same location are subjected to the SHPB uniaxial impact failure test; the damage evolution process of the specimen is comprehensively revealed from the two aspects of surface crack and fragment characteristics. Specifically, coal and rock samples are prepared from the coal seams, direct roof and direct bottom strata of the east fifth north wing heading face of the Sihe Coal Mine, which is seriously affected by coal and rock dynamic disasters. Then, based on HS–DIC technology and the mass screening method, the evolution laws of surface cracks during crushing and distribution characteristics of sample fragments after crushing are studied from the perspective of fractals, and the correlation between the two is explored to comprehensively reflect the impact damage processes of coal and rock. Finally, the Holmquist–Johnson–Cook (HJC) and Riedel–Hiermaier–Thoma (RHT) dynamic damage simulation models are established to reproduce the crack evolution process and verify the test results. The research is expected to further reveal the failure mechanisms of coal and rock materials under impact loading, and provide support for prewarning of coal and rock dynamic disasters.

2. Materials and methods

2.1. Material introduction and specimen preparation

As illustrated in figure 1(a), the experimental specimens were taken from the Sihe Coal Mine of Jinneng Holding Equipment Manufacturing Group Co., Ltd, which was seriously affected by coal and rock dynamic disasters. The east five north wing heading roadway in the Sihe Mine was a double tunneling working face, and the sampling point was located at the end of the No. 1 heading face (shown in figure 1(b)). According to the stratigraphic logging records of the boreholes near the sampling point shown in figure 1(c), coal seam #3 was in the Shanxi Group of the Lower Permian System, with silty mudstone on the direct roof and siltstone on the direct floor. To ensure the consistency of the coal and rock media, a hydraulic drilling rig was used to core the coal seams, direct roof strata and direct floor strata in the same area. The field sampling diagram of roof rock is shown in figure 1(d).

To minimize the inertial effect of the test piece and meet the internal stress homogenization assumption, by referring to the relevant research results [57–60], the samples were made into cylinders with dimensions of 50 mm diameter and 30 mm height. According to the suggested method for dynamic tests [61], the upper and lower surfaces of the specimen were precisely polished to ensure that the nonparallelism of the two ends of the cylinder was less than 0.05 mm, and the nonperpendicularity of the circumference and end face was less than 0.25°. As shown in figure 2, the samples were processed into eight cylindrical coal seam, roof rock stratum and floor rock stratum specimens, defined as C1–8, RR1–8 and FR1–8, respectively.

2.2. Test apparatus and test methods

2.2.1. Test system. Figure 3 illustrates the SHPB system developed by China University of Mining and Technology (Beijing). As illustrated in figure 3(a), the system consists of a dynamic system, bar system and data measurement system. (1) The dynamic system, i.e. the stress wave generator, is initiated by high-pressure nitrogen. The gases with different pressures drive the bullet to impact the incident bar and finally make the stress wave act on the specimen along the bar system. (2) The bar system, considering the large particle size and local anisotropy of coal and rock media, adopts an incident bar and transmission bar with a relatively large diameter ($\varphi = 50$ mm) and a length of 3000 mm and 2500 mm, respectively. During the test, the bar system should be at the same horizontal position to ensure the integrity of the test waveform and the accuracy of the data. (3) The data measurement system includes velocity measurement, strain measurement and HS photography subsystems, which are relatively complex. The velocity measurement subsystem consists of a parallel light source and a velocity tester. The photoelectric method is used to measure the velocity. That is, the instantaneous velocity of the impact bar is determined by the distance between two light sources and the truncation time difference. The velocity

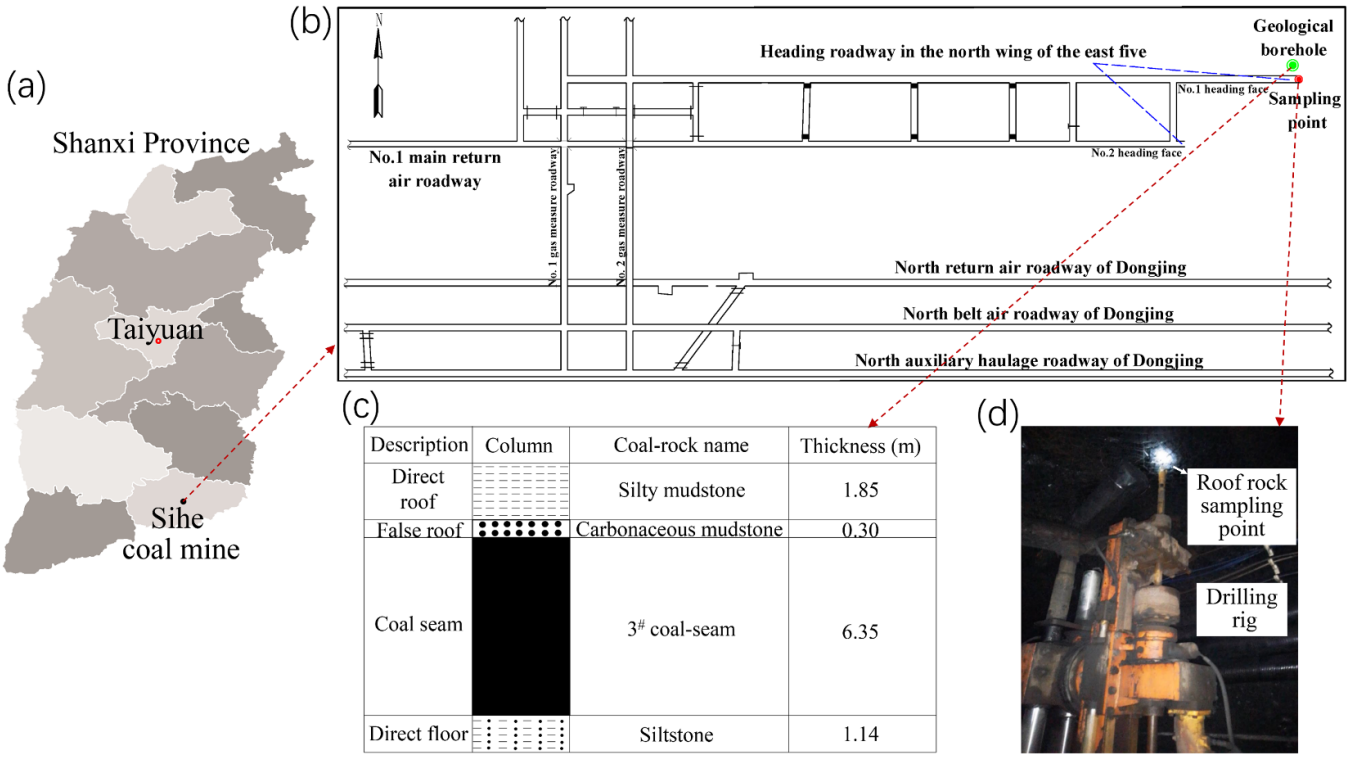

Description	Column	Coal-rock name	Thickness (m)
Direct roof		Silty mudstone	1.85
False roof		Carbonaceous mudstone	0.30
Coal seam		$3^{\#}$ coal-seam	6.35
Direct floor		Siltstone	1.14

Figure 1. Schematic diagram of coal and rock sampling: (a) location of the Sihe Coal Mine; (b) plan of mining roadway in the north wing of the east five; (c) stratigraphic logging records; and (d) field sampling figure of roof rock.

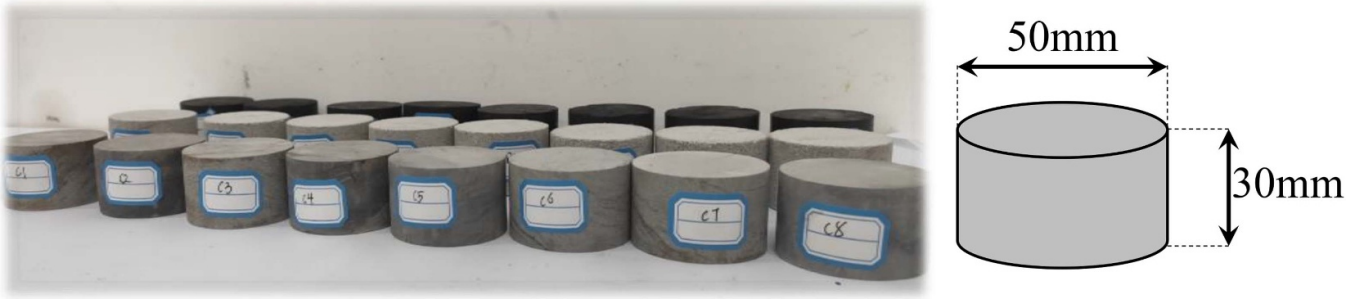

Figure 2. Illustration of coal and rock specimens.

tester is connected to the data acquisition system of the SHPB test, and the system automatically obtains the initial velocity of the impact bar and records its value. The strain measurement subsystem includes a semiconductor strain gauge, super dynamic strain gauge, waveform collector and data acquisition system. Two strain gauges, MC-AF-120, with a sensitivity of $(110 \pm 5)\%$, are pasted on the input bar and output bar to record the electrical signals during the test. The output signal of the strain gauge is collected by the LK2107A super dynamic strain gauge, displayed and stored on the DPO72004C oscillograph recorder produced by Tektronix Company, USA. The oscillograph recorder is connected to a computer to read, store and process signals.

Notably, to accurately depict the failure forms and crack evolution laws of coal and rock during SHPB impact, the HS photography subsystem is highlighted in figure 3(b). The main body of this subsystem is the GX-3 HS camera produced by NAC Company, Japan. The acquisition resolution is 1280 × 1024 pixels, with a pixel size of 21.7 μm, and the shooting frequency is 10 000 frames/second. The video data of the specimen under the impact of dynamic loading from beginning to end are recorded. Due to the particularity of coal and rock medium materials, the VL300W constant fill light produced by Godox Company, Shenzhen, China, is used in the experiment. The colour temperature adjustment range is 5400–5800 K, and the maximum illumination in the standard lampshade state is 77 000 $\mathrm{LUXm^{-1}}$. The light has a strong spotlight effect and colour fidelity to display more details during coal and rock damage and crack evolution. In addition, to effectively collect the specimen fragments, a plexiglass sleeve with a thickness of 2 mm is set outside the sample. The angles and positions of the sleeve, fill light and camera are adjusted many times to minimize the impact on the acquisition of speckle photos.

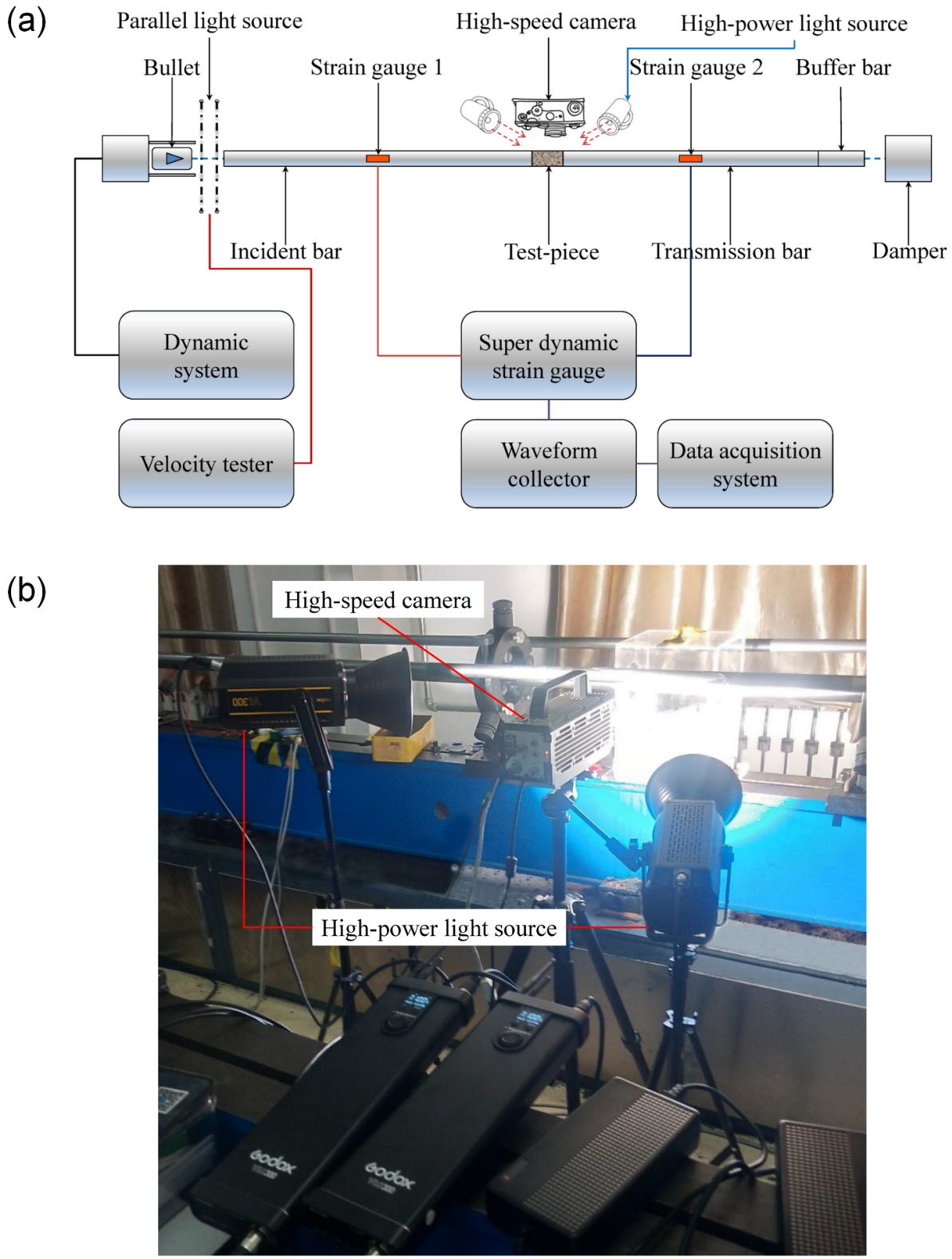

Figure 3. SHPB experimental system diagram: (a) a schematic view of SHPB system and (b) physical map of the high-speed photography subsystem used in the experiment.

2.2.2. Principles of the SHPB test. In stress wave propagation theory, the specimen in the SHPB impact experiment produces one-dimensional (1D) strain states, which is different from the 1D stress states of the tested materials in the low strain rate experiment [7]. Specifically, in the 1D strain states, the bullet is emitted from the chamber and hits the incident bar. The stress pulse is transmitted from the incident bar to the contact surface between the bar and the sample as a compression

wave. Due to the significant difference in wave impedance values, the reflected tensile wave is generated at the interface, accompanied by a transmission wave. Similarly, reflection and transmission occur at the interface between the sample and the transmission bar. After multiple reflections and transmissions, stress−strain equilibrium is achieved at the two end faces of the sample. The bars selected in this experiment are homogeneous materials with the same cross-sectional area as the coal and rock specimens. The incident wave, transmission wave and transmission wave signals recorded by the strain gauge are combined with the 1D stress wave theory and the three assumptions of the SHPB test to simplify the three-wave formula, thus obtaining the variations in the stress, strain and strain rate values of coal and rock samples with time [62]:

$$\sigma(t) = E_0\varepsilon_{\mathrm{t}}(t) \tag{1}$$

$$\varepsilon(t) = -\frac{2C_0}{L}\int_0^t \varepsilon_{\mathrm{r}}(t)\mathrm{d}t \tag{2}$$

$$\dot{\varepsilon}(t) = -\frac{2C_0}{L}\varepsilon_{\mathrm{r}}(t) \tag{3}$$

where $\dot{\varepsilon}(t)$, $\varepsilon(t)$ and $\sigma(t)$ are the loaded strain rate, loaded strain and loaded stress for the specimen, respectively; $\varepsilon_{\mathrm{r}}(t)$ and $\varepsilon_{\mathrm{t}}(t)$ correspond to the reflected wave strain and transmitted wave strain, respectively; E_0 and C_0 are the elastic modulus and wave velocity of the bar, respectively, and these two values are determined when the bar is determined; and L is the length of the specimen.

2.2.3. Box dimension calculation model. Many studies indicate that within a certain scale range, the surface cracks of brittle heterogeneous materials, such as coal and rock, show fractal characteristics to some extent, and fractal theory is applicable to quantitatively study parameters, such as crack morphology [63–66]. Among the common fractal dimension representation methods, the box dimension is the most widely used. The method has high practicability and accuracy and meets the requirements of computational efficiency and dynamic characteristics [67].

The principle of the box dimension [68, 69] is to cover coal and rock cracks with boxes composed of squares (boundary length of δ), and the number N_δ of nonempty boxes containing relevant crack pixels is counted. Obviously, there are significant differences in the number of N_δ values under different box sizes δ [70]. By changing δ, the statistical expression of fractal dimension D is as follows:

$$N_\delta = a\delta^{-D} \tag{4}$$

where a is the prefactor in the fractal dimension scaling rule. For a fixed crack image, a is a constant. If equation (4) is expressed in logarithmic form, the new expression is as follows:

$$\ln N_\delta = \ln a - D\ln\delta. \tag{5}$$

According to equation (5), the slope of $\ln N_\delta$ relative to $\ln\delta$ is obtained by linear regression, and the result is the fractal dimension D of the coal and rock surface crack image.

To ensure the accuracy of the calculation results, it is necessary to preprocess the image to eliminate the artefacts, noise and other noncrack elements in the original image recorded by the HS camera and reveal the real characteristics of cracks in the image. In this paper, Ratsnake annotation software [71] with high accuracy and resolution is used to manually extract cracks. Then, the crack sketch results are input into the FracLac plug-in on ImageJ software for box fractal dimension analysis. The flow chart is shown in figure 4. Ratsnake software and the FracLac plug-in are integrated to realize quantitative descriptions of surface cracks in coal and rock samples. In particular, ImageJ software evaluates whether the crack sketch is a binary image. If it is a binary image, the FracLac plug-in is manually opened for analysis. Otherwise, the image is binarized by setting a threshold. In Fraclac, the parameters of the control panel to analyze the cracks are set in the region of interest (ROI). Finally, the box fractal dimension is obtained by image scanning and the statistical results of equation (5).

2.2.4. Mass–frequency relationship model. In fact, fractal theory is used to describe the crack propagation laws of coal and rock during failure and to analyze the block size distribution characteristics after failure [72, 73]. Since the number of broken blocks is difficult to count, a screening test is carried out. To realize the quantitative expression of the degree of coal and rock fragmentation, Mandelbrot [74] and Zhao *et al* [75] established a mass–frequency relationship model based on the screening method, as shown in equation (6):

$$M(\varepsilon)/M = (\varepsilon/\sigma)^{3-D} \tag{6}$$

where ε is the pore size of the splitting sieve; σ is the average scale; $M(\varepsilon)$ is the mass of the broken body of coal and rock with a diameter less than ε; M is the total mass of the broken body of coal and rock; and D is the fractal dimension of mass. Obviously, the relationship between $M(\varepsilon)$ and M is expressed by the cumulative mass percentage of each particle size under the sieve.

By taking the logarithms of the left and right sides of equation (6) and sorting them out, we obtain the following equation:

$$D = 3 - \frac{\lg[M(\varepsilon)/M]}{\lg(\varepsilon/\sigma)}. \tag{7}$$

According to equation (7), in the double logarithmic coordinate system composed of $\lg[M(\varepsilon)/M]$ and $\lg(\varepsilon/\sigma)$, we use the least square method to fit the data and then subtract the slope of the straight line from 3, and the calculation result is the mass fractal dimension D.

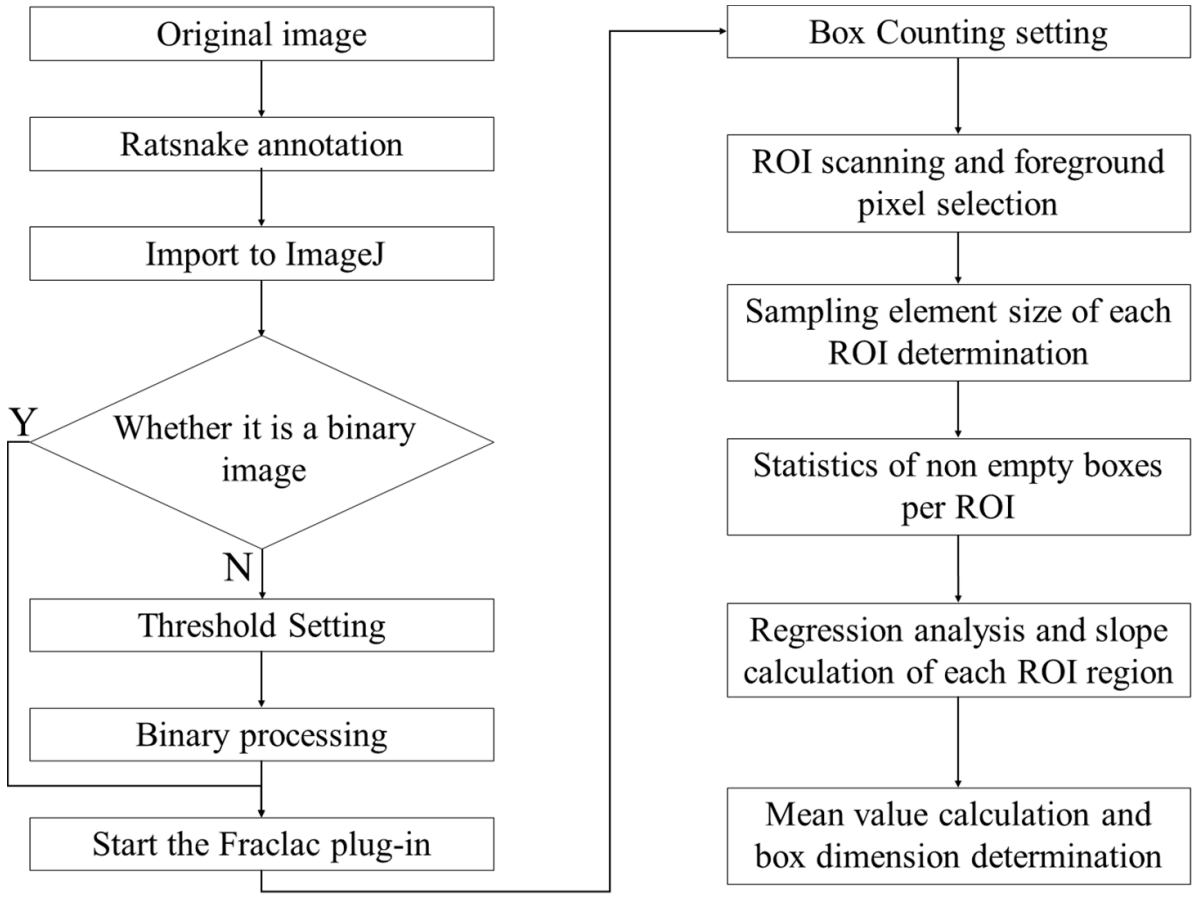

Figure 4. Calculation flow chart of the box dimension.

3. Test results and discussion

3.1. Dynamic mechanical characteristics

3.1.1. Test results of physical and mechanical parameters. To facilitate comparative analysis, two specimens were selected from each group of coal and rock samples for the following experiments: (1) the uniaxial compression failure test based on an electrohydraulic servo testing machine and (2) the porosity measurement experiment based on the mercury intrusion method. In this process, some basic physical and mechanical parameters, such as the uniaxial compression coefficient, elastic modulus, Poisson's ratio and porosity, were measured. In addition, to reflect the compactness of the sample, a ZBL-U510 nonmetallic ultrasonic detector produced by Beijing Zhibo Lian Technology Co., Ltd was selected to conduct a single-emission and single-receiving acoustic transmission test on the remaining specimens [76] with reference to the test method specified in ASTM D 2845 [77]. The arithmetic mean of the longitudinal wave velocity was calculated after multiple tests. The results are summarized in table 1.

Relative to the results of the ultrasonic longitudinal wave velocity test of coal, roof rock and floor rock specimens in the Sihe Mine shown in table 1, although the data have some dispersion, the longitudinal wave velocity in each group is basically similar; this phenomenon reflects the high homogeneity characteristics of the collected and prepared samples, providing scientific support for subsequent analysis. In addition, by comparing the longitudinal wave velocities of different samples, the values of rock samples are significantly greater than those of coal samples, and the values of floor rock samples are generally slightly greater than those of roof rock samples. By comprehensive comparisons of the above physical and mechanical parameters, although coal and rock are both elastoplastic materials, the former is significantly denser and more prone to brittleness. In comparison, the plasticity and ductility yield of coal are more prominent.

3.1.2. Dynamic stress equilibrium. After testing the ultrasonic longitudinal wave velocities of coal and rock samples, we conduct 18 groups of impact load tests. The specific experimental parameters are shown in table 1 in section 3.1.1. The impact speed ranges from 4 m s^{-1}–14 m s^{-1}, and each 2 m s^{-1} increase is set as a speed step, which is divided into six levels. After each SHPB test, to ensure the accuracy of the results, the stress equilibrium at both sides of the rock specimen requires careful checking. Figure 5 shows the typical dynamic stress equilibrium states, which are obtained from the floor rock sample (FR4) with an impact velocity of 8.885 m s^{-1}. According to the SHPB test principle, the stresses at both ends of the sample are calculated from the test signals on the elastic bar.

Table 1. Test results of coal and rock samples.

Sample category	Sample ID	Density ρ (g cm^{-3})	P wave velocity v (km s^{-1})	Uniaxial compressive strength f_c (MPa)	Elastic modulus E (GPa)	Poisson's ratio ν	Porosity n (%)	Impact speed v (km s^{-1})	Experimental result
Coal samples	C1	1.224	0.62	—	—	—	—	4.231	Impact fracture
	C2	1.255	0.70	—	—	—	—	5.698	Impact fracture
	C3	1.203	0.59	—	—	—	—	7.093	Impact smash
	C4	1.229	0.72	—	—	—	—	9.356	Impact smash
	C5	1.230	0.68	—	—	—	—	11.993	Impact smash
	C6	1.220	0.58	—	—	—	—	13.412	Impact smash
	C7	—	—	18.57	4.31	0.32	—	—	Static-load fracture
	C8	—	—	—	—	—	8.67	—	—
Roof rock samples	RR1	2.320	2.04	—	—	—	—	4.377	Impact fracture
	RR2	2.290	1.75	—	—	—	—	6.213	Impact smash
	RR3	2.348	1.72	—	—	—	—	7.110	Impact smash
	RR4	2.327	1.86	—	—	—	—	9.213	Impact smash
	RR5	2.327	1.94	—	—	—	—	11.947	Impact smash
	RR6	2.280	1.73	—	—	—	—	14.013	Impact smash
	RR7	—	—	41.26	8.37	0.21	—	—	Static-load fracture
	RR8	—	—	—	—	—	1.41	—	—
Floor rock samples	FR1	2.546	1.37	—	—	—	—	4.668	Impact fracture
	FR2	2.473	1.83	—	—	—	—	5.516	Impact smash
	FR3	2.475	2.33	—	—	—	—	8.582	Impact smash
	FR4	2.385	2.50	—	—	—	—	8.885	Impact smash
	FR5	3.057	2.32	—	—	—	—	11.865	Impact smash
	FR6	2.505	2.65	—	—	—	—	13.877	Impact smash
	FR7	—	—	40.57	8.26	0.25	—	—	Static-load fracture
	FR8	—	—	—	—	—	1.53	—	—

Specifically, the superposition of the incident wave and reflected wave reflects the stress at the incident end of the sample; the transmitted wave reflects the stress at the transmission end. Figure 5 shows that the curves at both ends are basically coincident, which indicates that the specimen is in a state of stress equilibrium during the dynamic loading process.

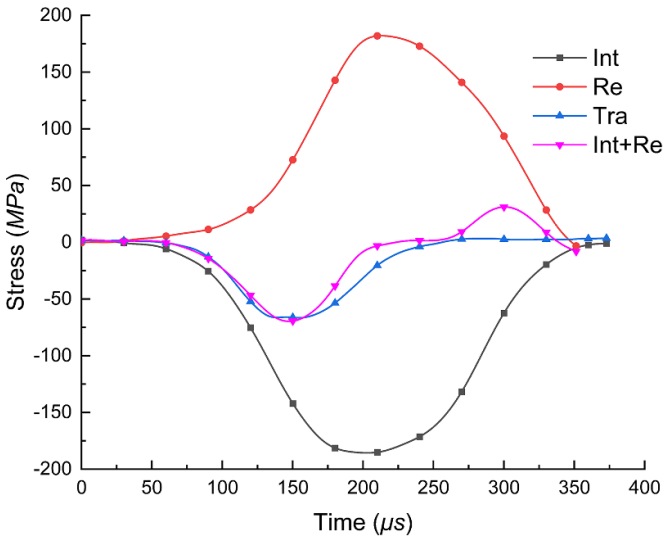

Figure 5. Typical dynamic stress equilibrium checks in dynamic compression tests (Int: incident wave, Re: reflected wave, and Tra: transmitted wave).

3.1.3. Time history curve of stress wave and signal denoising. In the SHPB impact damage experiment of coal and rock, semiconductor strain gauges are arranged on the input bar and output bar to capture the incident wave, reflected wave and transmitted wave. Then, the signals are stored through a super dynamic strain gauge, waveform collector and data acquisition system. As space is limited, by taking the impact test with a speed level of 6 m s^{-1} as an example, the time history curve of the stress waveform is displayed in figure 6(a). The figure shows that each waveform roughly presents a half-sine curve, and the dispersion of the waveform and the resulting wave head oscillation are effectively suppressed. However, the original waveform signals in figure 6(a) contain a large amount of noise interference, which is particularly evident in the transmitted wave. This phenomenon is caused by external environmental impact and Pochhammer–Chree (PC) oscillation [78]. Due to high noise, short duration and rapid mutation, the waveform signal generated by the impact dynamic load is a nonstationary signal, which can be denoised by the Hilbert–Huang transformation (HHT) method [79, 80]. The denoised

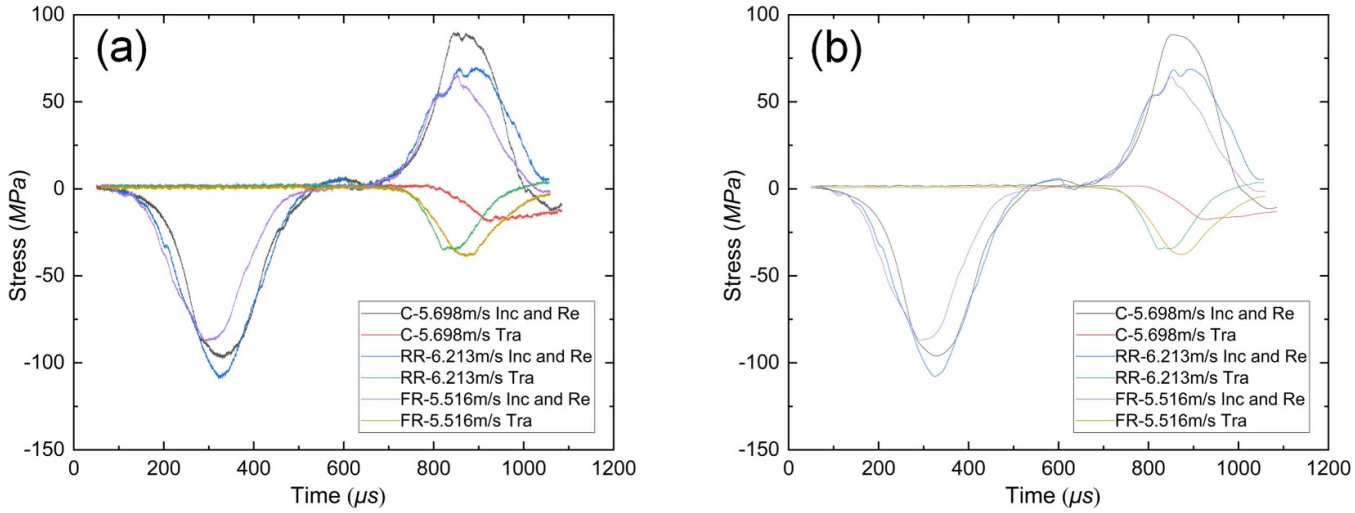

Figure 6. Time history curves of stress waves at 6 m s^{-1} impact velocity level: (a) original curves and (b) denoised curves.

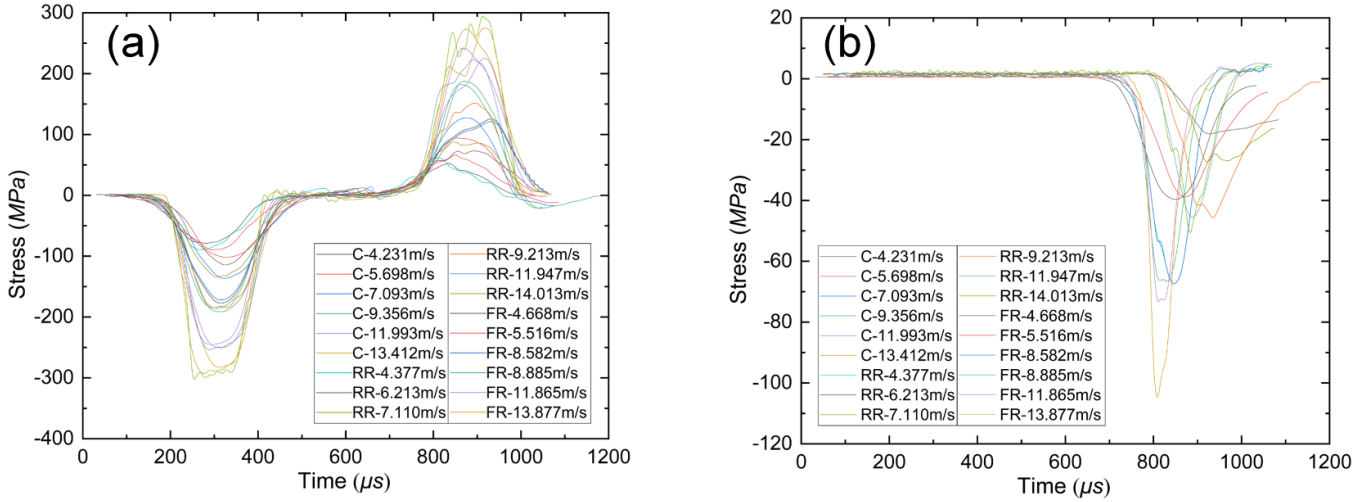

Figure 7. Denoised stress wave signals at different impact velocities: (1) incident-reflected waves and (2) transmitted waves.

signal is shown in figure 6(b). Relative to figure 6(a), the signal amplitudes before and after filtering have little changes; however, high-frequency noise is effectively eliminated, and the signal-to-noise ratio is significantly improved.

Similarly, 18 groups of stress waves are filtered and denoised, and the time history curves of incident-reflected waves and transmitted waves are shown in figure 7. Figures 7(a) and (b) show that with increasing impact speed, the stress wave amplitudes of coal and rock impact is increased, the time to the peak is advanced, and the overall duration of the stress wave is gradually shortened. Most notably, in figure 7(a), when the impact velocity is low, negative values appear at the tail end of the reflected wave. The reason for this phenomenon is that the specimen is not destroyed completely under incident wave loading conditions, and a large amount of strain energy is stored in the medium instead. These strain energies are released in the unloading phase of the incident wave and rebound to the bar as compression waves. In contrast, when the impact velocity is high, the coal and rock samples are destroyed instantaneously under the action of the incident wave, and the compression rebound in the reflected wave disappears.

In addition, at similar impact velocities, the stress waves of each coal and rock specimens have high coincidence. The peak values of the incident wave and transmission wave of the coal samples are lower than those of the rock samples; however, the reflected waves are higher. Similarly, when the test sample is coal, the time to the peak is often relatively slow. According to a comparison of the ultrasonic longitudinal wave velocity test results in table 1, denser samples have faster stress wave propagation speeds. In conclusion, the time history curve of the stress wave is affected by both the impact velocity and the physical properties of the sample.

3.1.4. Dynamic mechanical characteristics of coal and rock during impact. According to equations (1)–(3), the time−strain rate, time−strain and strain−stress relationships under different impact speeds are calculated, and the results are shown in figure 8. Figure 8(a) compares the change rule of

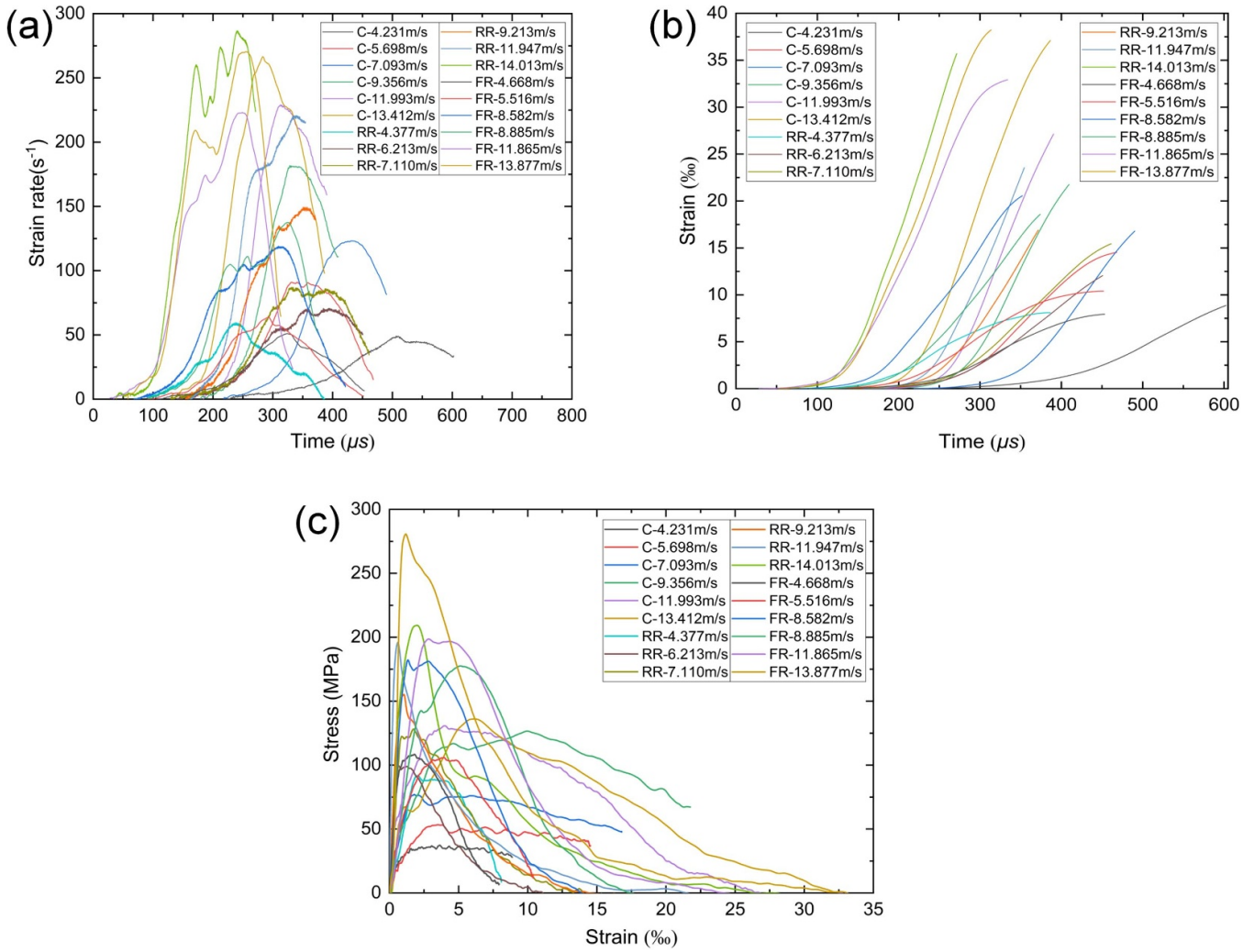

Figure 8. Dynamic mechanical characteristic curves of coal and rock impact: (a) time−strain rate curves; (b) time−strain curves; and (c) strain−stress curves.

the strain rate with time at different speeds. When the impact speed is low, the strain rate curve slowly increases to the peak point and then gradually decreases. With increasing impact velocity, the slope value of the strain rate curve increases rapidly, the end position of the curve gradually approaches the peak point, and there is a short fluctuation in the peak section. Figure 8(b) shows the time−strain curves. With the increase in impact speed, the times for initial strain and failure instability characteristics of coal and rock materials are significantly shortened. At similar impact velocities, the jumping points of the strain curves of rock samples are earlier than those of coal samples, and the cut-off time of the strain curves of roof rock samples are earlier than those of coal samples and floor rock samples in most cases. The reasons for this phenomenon are as follows. (1) Although rock and coal are both elastic−plastic complexes, the former is more inclined to show its brittleness, while the latter has more prominent plasticity and ductility. (2) The crack derivation and damage failure characteristics of roof rock samples are obviously faster than those of floor rock samples, which needs to be verified by subsequent test results. Figure 8(c) shows the relationships between strain and stress at different impact velocities. When the impact speed is small, the initial slope of each sample curve has little difference. After entering the plastic stage, the curve slowly drops from the peak stress, and vibration and fluctuation occur. With the increase in impact, the initial rates of coal and rock samples gradually coincide, and each curve first drops and then rebounds after reaching the first peak, showing a saddle shape, which is obviously a manifestation of strain strengthening. At a higher strain rate, the sample reaches the stress peak at a smaller strain, and its brittleness is more obvious.

3.2. Process of crack propagation and specimen failure

3.2.1. Recognition and feature extraction of surface cracks. To date, many scholars have used HS cameras to record the evolution laws of surface cracks and explore the failure processes of coal and rock masses. Image processing is a prerequisite for crack analysis, especially for coal and rock samples with low contrast and robustness between cracks and specimens. The floor rock sample (FR1) is taken as an example, and its impact velocity is 4.668 m s^{-1}. FR1 takes 29 ms from the

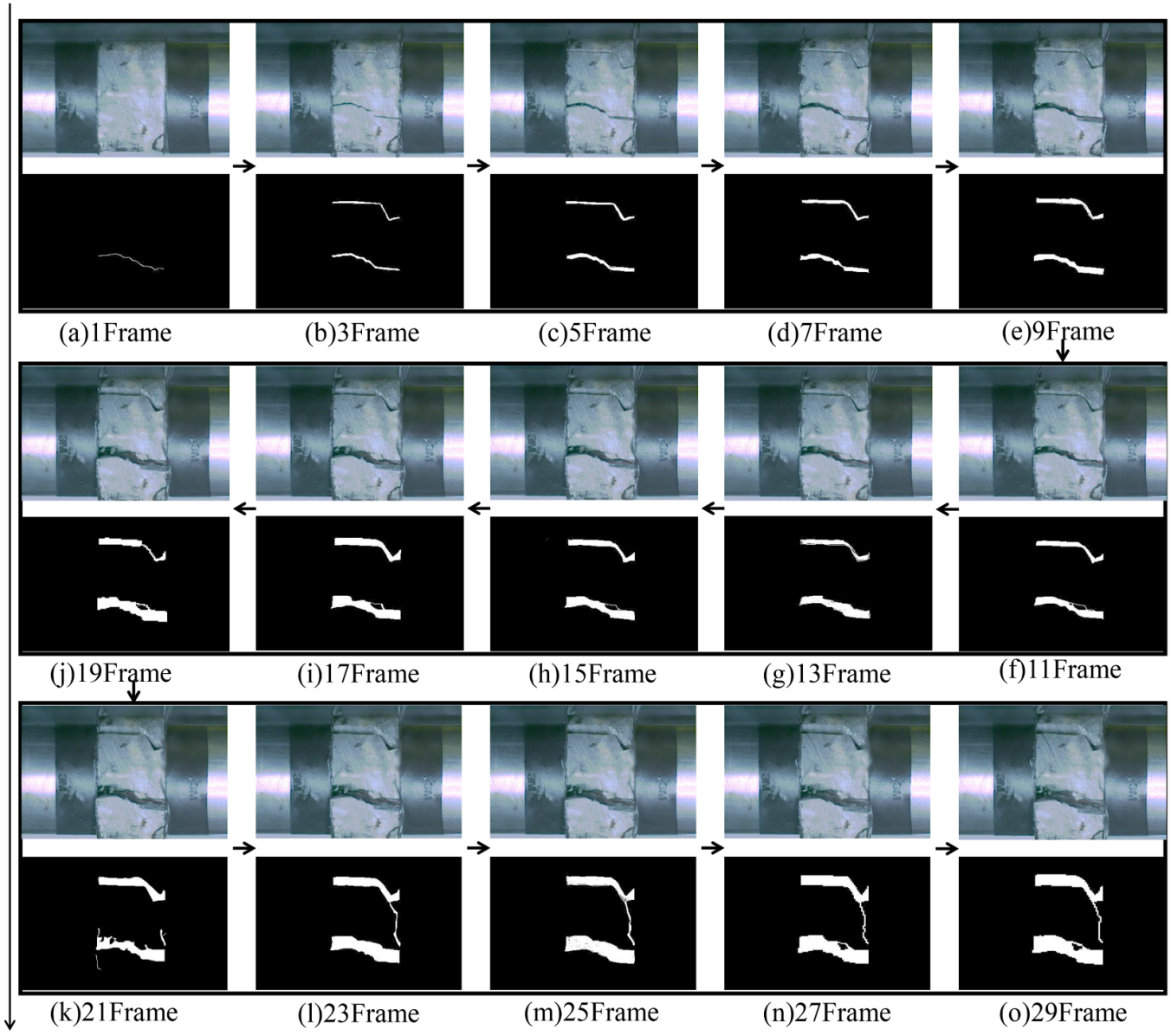

Figure 9. Original crack images and ratsnake software extraction results.

contact between the incident bar and the sample to the ejection of rock fragments. The HS camera shoots at a frequency of 10 000 frames s^{-1} and extracts pictures every 2 ms, obtaining 15 pictures. Ratsnake is utilized to annotate the cracks in each image, and the analysis results are shown in figure 9.

Figure 9 shows the crack evolution process of the FR1 sample under the impact load of the SHPB, as follows: (1) The crack first occurs in the middle of the sample, and the main radius direction of the crack equivalent ellipse [24] is basically 45° oblique to the impact loading direction of the axis. (2) The crack rapidly extends to both ends of the sample, and another parallel main crack appears in other areas. (3) Both main cracks continue to expand, accompanied by the simultaneous generation of minor cracks. Relative to the main crack, the propagation direction of the minor crack has great randomness. (4) As the impact continues, the main cracks and the minor cracks expand synchronously, and the area and pixel ratios of the cracks increase. By the 29-frame shooting time, fragments are ejected, and the identification and analysis of surface cracks are terminated.

3.2.2. Crack quantification and box dimension calculation. Based on the Ratsnake surface crack identification results, according to the box dimension calculation model, the FracLac plug-in is used to operate and process the crack patterns in the SHPB impact failure of each coal and rock specimens to quantitatively depict the evolution law of each sample from crack generation to fragment ejection. According to the flow chart shown in figure 4, a total of 75 coal seam sample fractal dimensions, 60 roof rock fractal dimensions, and 73 floor rock fractal dimensions are obtained through linear regression and average value calculation. The above results are summarized, and the box dimension progress curves of coal and rock samples are drawn, as shown in figure 10.

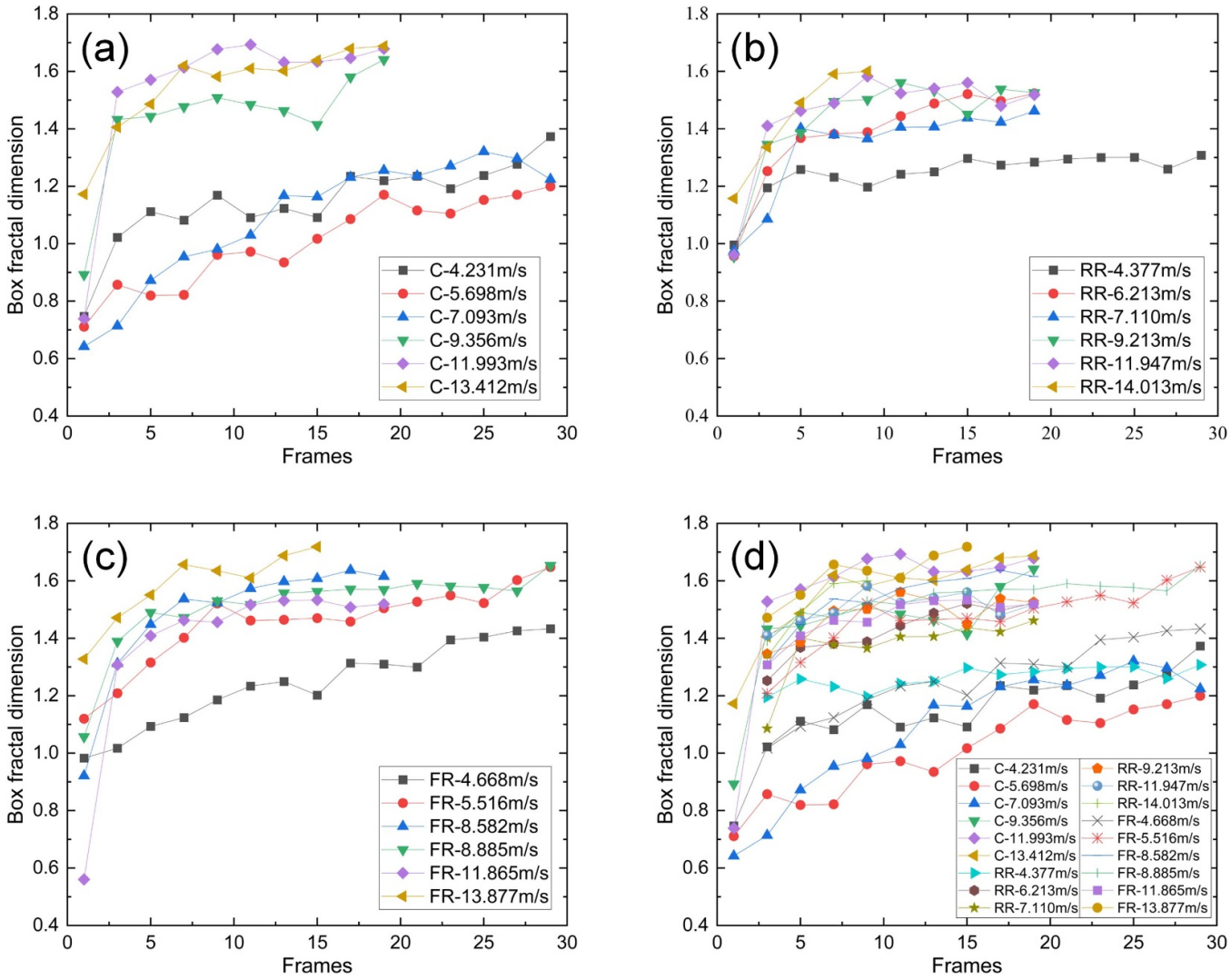

Figure 10. Box dimension evolutions of cracks in coal and rock specimens: (a) coal samples; (b) roof rock samples; (c) floor rock samples; and (d) all samples.

The box dimensions of surface cracks of coal samples, roof rock samples, and floor rock samples under different SHPB impact velocities are shown in figures 10(a)–(c), respectively. Three diagrams show similar evolution characteristics. (1) For impact failure at a specific speed, the box dimension of the coal and rock specimens shows the laws of overall increase and local oscillation. The reason for the overall increase is obvious: the box dimension itself is a quantitative reflection of the whole process, from crack expansion to the overall failure of the specimen with impact. The local oscillation fully reflects the complexity, heterogeneity, and anisotropy characteristics of coal and rock materials, and the crack may still be closed during the overall growth. (2) Generally, the growth rate of the box dimension is relatively fast at the initial stage, while the subsequent increasing trend is slowed. Rapid crack initiation occurs immediately when the incident bar hits the specimen. Relative to the initial incident wave, the damage levels of the reflected tensile wave and subsequent superimposed wave on the specimen are weakened. (3) With increasing impact velocity, the slope of the box dimension curves of surface cracks in coal and rock specimens increase synchronously; however, the duration is continuously shortened. The results show that a higher impact velocity promotes the damage process, significantly accelerates crack evolution, and greatly advances the ejection times of coal and rock fragments.

Additionally, as shown in figure 10(d), we have purposely compared the box dimension differences of coal and rock samples. First, the variation trend of the box dimension of the roof rock sample is similar to that of the floor rock sample. Second, under a similar impact velocity, the rock sample oscillation degree is more intense than that of the coal sample. Third, the numbers of crack evolution images of roof rock samples captured by a high frame rate camera are relatively less than those of coal and floor rock samples. The curve durations of most roof rocks are relatively short, which is a prominent reflection of the rapid transition of the sample from the initial derivations of cracks to the ejection state of fragments. Finally, when the impact velocity is low, the box dimensions of the rock samples are larger than those of the coal samples. When the impact speed is high, the opposite is

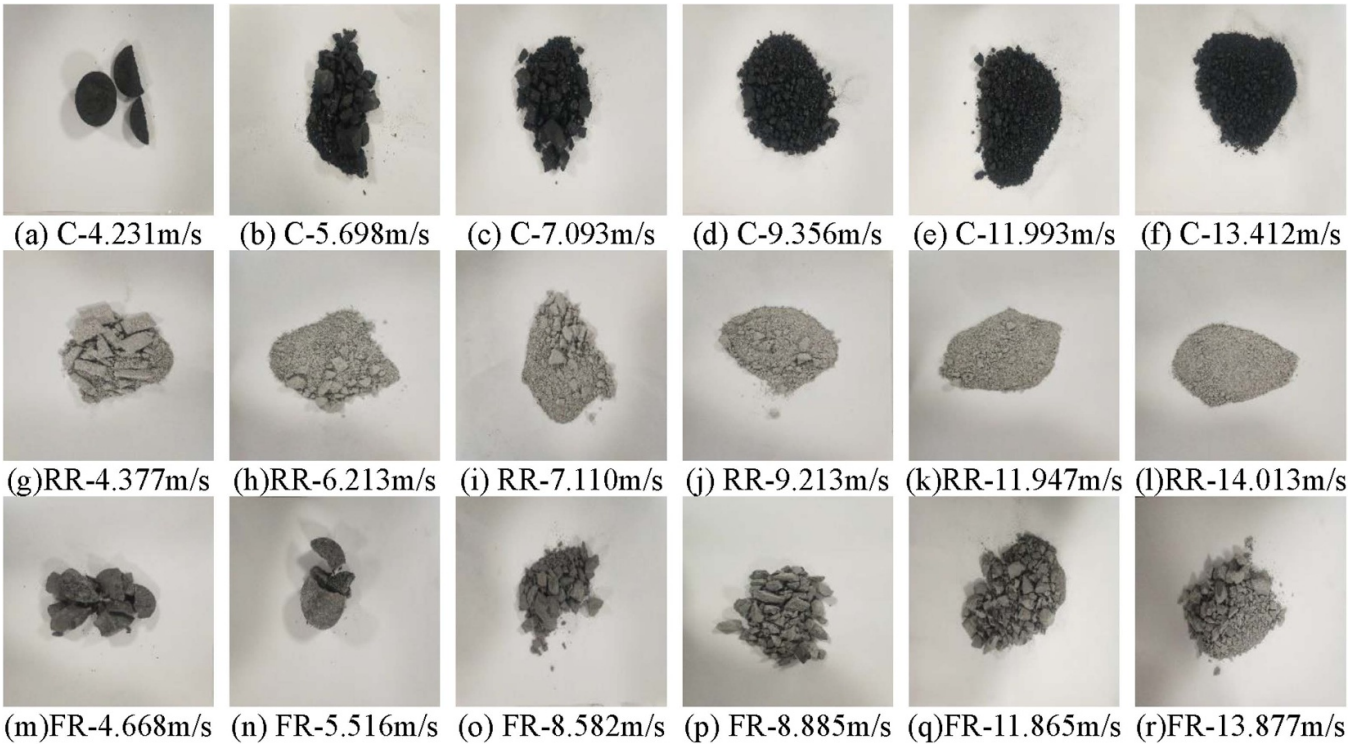

Figure 11. Failure modes of coal and rock specimens under different strain rates.

true. The results indicate that for the prepared test pieces, the rock samples show more apparent heterogeneity and impact resistance levels (i.e. the ability to resist damage) than the coal samples. In other words, as elastic−plastic complexes, most rock samples show brittle failure under the action of incident waves. During the impact failure of coal samples, the plastic characteristics are more obvious.

To quantitatively characterize the crack evolution law of the specimen, this paper adopts the research method of first using an HS camera to obtain the impact failure processes of coal and rock and then using the box dimension to conduct fractal analysis. There are three defects in this method. (1) The sketches of cracks are manually marked by Ratsnake. The cracks require a heavy workload, and the crack-filling situation and the fragment ejection cut-off criteria are subjective. (2) The failure observation surface of the specimen is bent. The plane picture is used to characterize the crack evolution law on the circumference face of the coal and rock mass. The normal direction of the cracks may have an angle with the analysis plane, producing corresponding result errors [23]. (3) The coal and rock samples are prepared as three-dimensional cylinders. As limited by the experimental conditions and equipment, we analyze the plane illuminated by the high-power projector, leading to the failure fully expressing the evolution of some cracks, which is the main reason for the error in figure 10(d). To compensate for the impacts of the above drawbacks on the analysis results, we select sample sieves with different apertures to fully screen the coal and rock fragments after impact and discuss impact damage from another perspective.

3.2.3. Fractal characteristics of crushing products. Figure 11 shows the fragment morphologies of coal and rock specimens collected under different strain rates after impact. The coal and rock specimens under impact loading have strong strain rate sensitivities [81]. Specifically, when the impact velocity is low, the coal and rock samples still maintain certain degrees of integrity, and most of them are in a massive dispersion state. With increasing impact speed, the damage degrees of coal and rock increase. For the broken body, the volume is significantly reduced, and the quantity is correspondingly increased. The failure form of coal and rock changes from fragmentation to pulverization [82].

With reference to relevant standards [83], sample sieves with 9.50 mm, 4.75 mm, 2.36 mm, 1.18 mm, 0.60 mm, 0.30 mm, 0.15 mm, and 0.075 mm apertures are selected for combination, and the coal and rock fracture sieves after SHPB impact damage are divided into eight grades. A high-precision balance is used to weigh the broken blocks of coal and rock of each grade. The statistical results are summarized in table 2.

As a note, since the coal sample (C1) is broken into three pieces after impact, which has no screening significance, the value is discarded. By referring to equation (7), the double logarithmic expressions of the impact samples are established, and the regression analysis is carried out. The results are shown in figure 12.

In table 2 and figure 12, there is a good logarithmic correlation between the cumulative mass percentage of the particle size under the sieve and the diameter of the sample sieve. The fractal dimension fluctuates between 1.1601 and 2.6029, and the fitting coefficient is relatively high, indicating that the

Table 2. Calculation results of the mass dimension.

Sample no.	Impact speed ($m\ s^{-1}$)	Cumulative mass percentage of each particle size under the sieve (%)								Fitting results			Fractal dimension
		0.075 mm	0.15 mm	0.30 mm	0.60 mm	1.18 mm	2.36 mm	4.75 mm	9.50 mm	Fitting slope	Intercept distance	Decision factor (R^2 Value)	
C1	4.231	—	—	—	—	—	—	—	—	—	—	—	—
C2	5.698	0.094	0.483	1.763	3.435	6.142	13.772	35.832	100.000	1.3283	0.0421	0.9796	1.6717
C3	7.093	0.191	0.651	2.007	4.406	8.731	20.448	43.140	100.000	1.2484	0.0821	0.9916	1.7516
C4	9.356	1.176	3.310	9.325	19.398	35.236	65.126	93.262	100.000	0.9342	0.2758	0.9461	2.0658
C5	11.993	1.333	4.247	12.777	25.264	43.906	71.486	90.506	100.000	0.8828	0.2877	0.9168	2.1172
C6	13.412	2.096	5.632	14.207	25.979	42.337	72.940	96.173	100.000	0.8036	0.2522	0.9349	2.1964
RR1	4.377	2.209	6.086	17.784	23.343	27.851	33.289	46.225	100.000	0.6703	0.0174	0.9034	2.3297
RR2	6.213	4.757	13.722	38.860	52.136	59.677	67.109	86.354	100.000	0.5565	0.1804	0.8176	2.4435
RR3	7.110	5.061	15.283	25.823	45.014	52.068	60.618	83.846	100.000	0.5532	0.1414	0.8884	2.4468
RR4	9.213	6.439	17.865	41.518	53.002	60.168	69.875	91.350	100.000	0.5006	0.1613	0.8309	2.4994
RR5	11.947	9.133	25.963	61.767	74.085	81.830	90.348	97.955	100.000	0.4245	0.1929	0.7248	2.5755
RR6	14.013	10.552	28.129	71.812	85.450	91.583	96.676	100.000	100.000	0.3971	0.2026	0.6755	2.6029
FR1	4.668	0.014	0.043	0.114	0.215	0.487	1.214	4.861	100.000	1.6148	−0.5618	0.9379	1.3852
FR2	5.516	0.000	0.011	0.032	0.071	0.141	0.379	0.839	100.000	1.8399	−0.8640	0.8471	1.1601
FR3	8.582	0.127	0.363	1.095	2.516	6.007	14.064	32.960	100.000	1.3399	0.0080	0.9980	1.6601
FR4	8.885	0.647	1.097	1.943	3.400	5.861	15.053	43.044	100.000	1.0396	−0.1018	0.9810	1.9604
FR5	11.685	0.688	1.960	3.802	6.799	12.263	27.329	62.509	100.000	1.0111	0.0692	0.9946	1.9889
FR6	13.877	2.476	4.681	8.385	12.510	18.450	32.966	64.208	100.000	0.7493	0.0146	0.996	2.2507

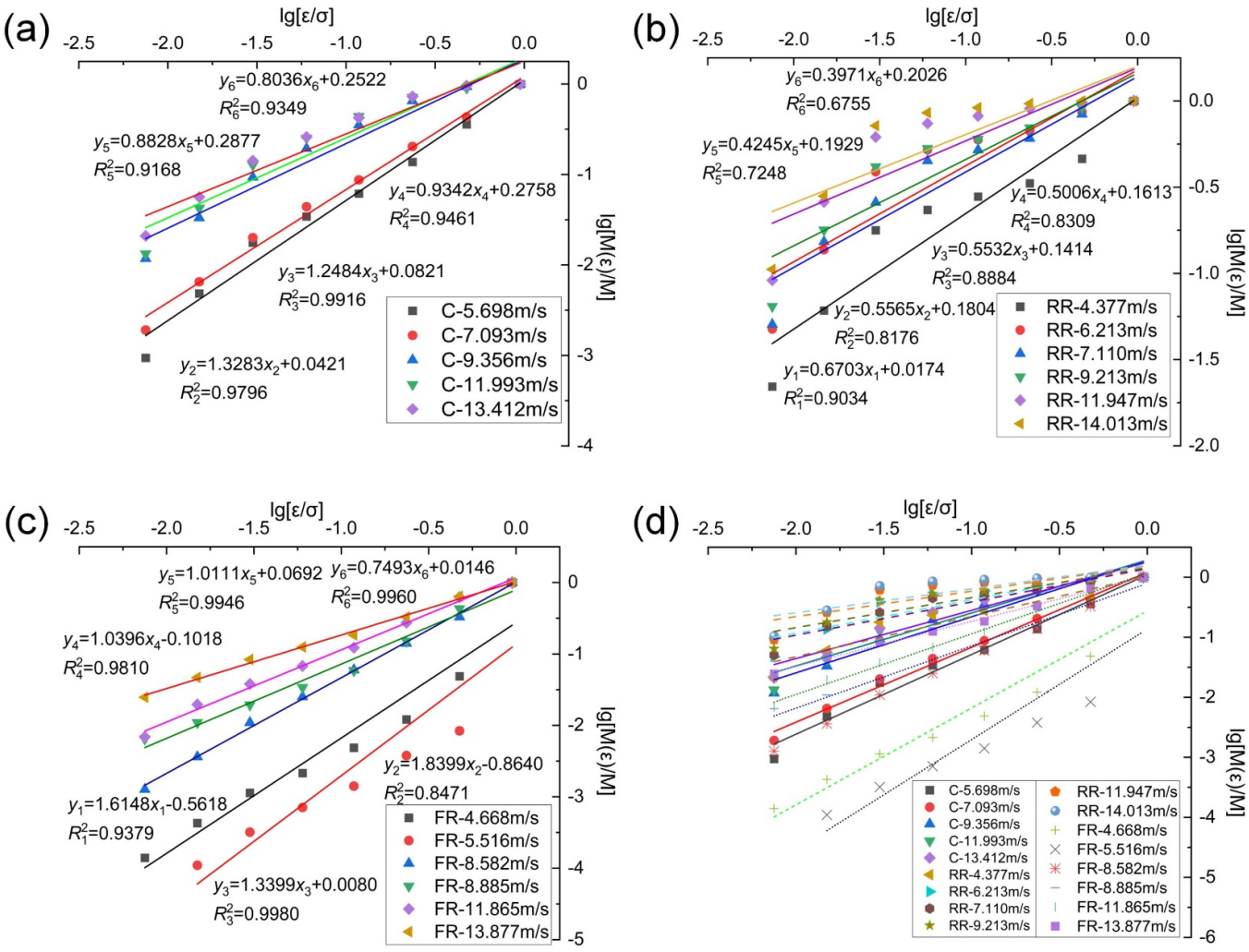

Figure 12. Statistical graphics of cumulative particle size distribution: (a) coal samples; (b) roof rock samples; (c) floor rock samples; and (d) all samples.

coal and rock fragmentation block has obvious self-similarity and fractal characteristics. In general, the slope of the fitting curve decreases with increasing impact velocity and strain rate. Accordingly, the fractal dimension increases, indicating that the fragmentation of coal and rock blocks gradually intensifies after impact. In addition, the fractal dimension of the roof rock sample under similar impact speed is larger than that of the floor rock sample; the block is broken more severely. Combined with the ultrasonic test results in table 1, the floor rock samples are generally denser than the roof rock samples, and they are also easier to preserve their structural integrity at similar impact speeds. The similar rules can be mutually corroborated with figures 10(d) and 11.

3.2.4. Correlation characteristics of the box dimension and mass dimension. The box fractal dimension is used to characterize the surface progressive fracture processes of coal and rock during impact, and the mass fractal dimension is employed to describe the distribution characteristics of fragments after impact. Obviously, exploring the correlation between these two fractal dimensions helps to understand the processes of coal and rock masses impact failure. The box fractal dimension is obtained from the analysis of specific crack images by HS–DIC technology, and there are significant differences in crack images at different times. For each coal and rock sample, we select the last frame image before fragment ejection and calculate its box fractal dimension. This value is compared with the mass fractal dimension, and the relationship between them and impact velocity is established, as shown in figure 13.

Figure 13(a) shows that both the box fractal dimension and mass fractal dimension are positively correlated with the impact velocity. From the perspective of energy, when the SHPB device is used for the impact test, the energy absorbed by the coal and rock specimen is mainly converted into breakage energy for crack propagation and the generation of a new fracture surface. With increasing impact speed, the breakage energy increases synchronously, producing the following results. (1) On the surface of the sample, the evolution of cracks is significantly promoted, and the number of cracks is greatly increased, increasing the box dimension. (2) In the

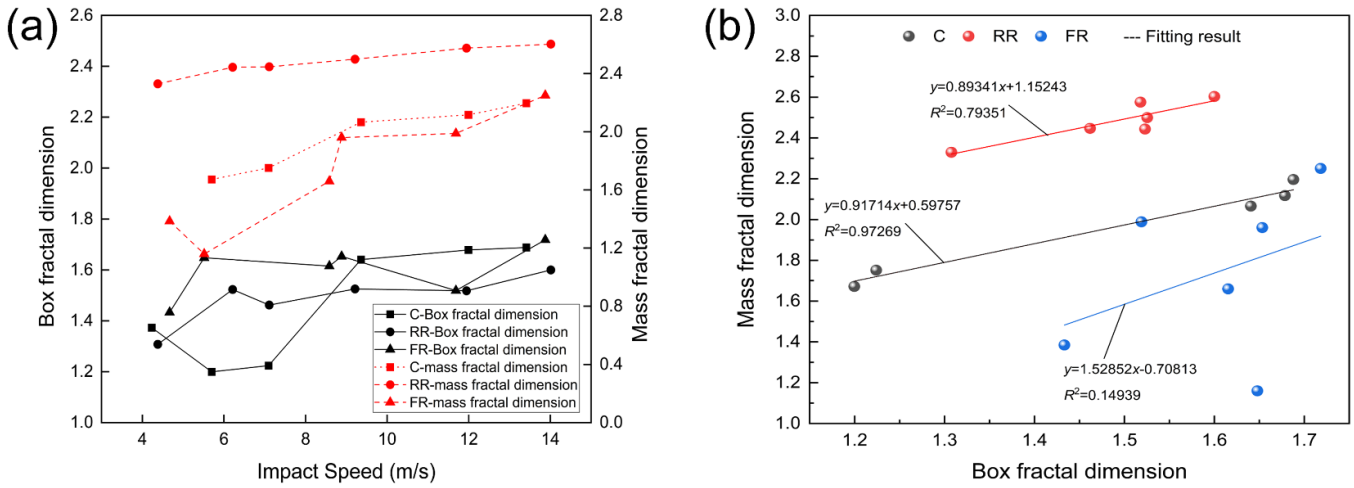

Figure 13. Relationship between the box dimension, mass dimension and impact velocity of coal and rock samples: (a) relationship between two dimensions and impact velocity and (b) relationship between two dimensions.

interior of the sample, the breakage energy converts into the surface energy of the newly broken fragments and intensifies the collision and friction between the fragments, further reducing the fragmentation of the broken body and finally leading to a synchronous increase in the mass dimension. In addition, in figure 13(a), the two curves of the box fractal dimension and mass fractal dimension are approximately parallel in some sections, indicating that there is a certain correlation between them. Therefore, we establish a scatter diagram of the box fractal dimension and mass fractal dimension under the same impact speed and carried out data fitting. The result is shown in figure 13(b). There is a positive linear correlation between the box fractal dimension and the mass fractal dimension. Specifically, the box fractal dimension and the mass fractal dimension are both quantitative characterizations of the impact failure of the specimen. As the box dimension increases, the mass dimension increases synchronously. In figure 13(b), the box fractal dimension is a planar description of the circumference face crack of the cylinder, which is a two-dimensional calculation of the surface crack. In contrast, the mass fractal dimension focuses on the failure patterns of the internal and external fragments of the specimen, which is a three-dimensional interpretation of the overall failure. The unification of the two is helpful for comprehensively reflecting the dynamic characteristics and failure processes of coal and rock under impact conditions. Notably, the two dimensions are different expressions of coal and rock damage, and there is a certain randomness of crack growth, which is the main reason for the large difference in the correlation coefficient (R^2 value) of the coal and rock material fitting curve in figure 13(b).

4. Numerical simulation of coal and rock impact failure

Earlier in the article, we systematically described the failure processes of coal and rock masses based on experimental results. However, the dynamic characteristics and crack evolution laws of coal and rock specimens under impact loads are extremely complex and are significantly different from those under quasistatic loads. In this case, the impact responses of heterogeneous materials, such as coal and rock, are usually determined by comparing laboratory tests with numerical simulations [84]. In the finite element simulation analysis of nonlinear dynamics, such as the HS impact of coal and rock, the LS-DYNA program launched by ANSYS, Inc. and Livermore Software Technology Corporation (LSTC) is widely used [85]. In this section, based on two dynamic damage constitutive models, HJC [86] and RHT [87], we have utilized the LS-DYNA program to simulate the impacts of coal and rock, compared the simulated crack evolution process with the experimental test results, revealed the overall process and internal mechanism of sample failure from the level of detail, and evaluated the impact of the constitutive model on the simulation results of coal and rock impact.

4.1. Simulation model establishment

4.1.1. HJC theoretical model. The constitutive model is the macroscopic representation of physical and mechanical properties and the basis of LS-DYNA material modeling. The HJC model is a computational constitutive model for coal and rock media with high strain rates and large strains and is especially suitable for both LaGrange and Eulerian codes. The HJC model exists in the MAT No. 111 material of LS-DYNA and contains 21 parameters. These parameters are classified into five categories: basic material parameters, material strength parameters, material damage parameters, material pressure parameters, and software parameters. According to the physical and mechanical properties of the coal and rock used in the experiment and by referring to the relevant literature [88–91], the HJC constitutive model parameters are determined as shown in table 3 (unit: g-cm-us system). In addition, the ADD_EROSION keyword has been added to the k-file to add a tensile damage failure criterion, i.e. MXEPS = 0.0005.

Table 3. Determination of the HJC constitutive model parameters.

	Basic material parameters				Material strength parameters					Material damage parameters			Material pressure parameters							Software parameters	
Media	ρ	f_c	G	T	A	B	C	N	S_{fmax}	D_1	D_2	E_{fmin}	K_1	K_2	K_3	P_c	u_c	P_l	u_l	E_{pso}	F_s
C	1.227	1.857×10^{-4}	0.016	4.31×10^{-6}	0.76	1.66	0.001	0.72	7	0.31	1	0.01	0.85	−1.71	2.08	6.19×10^{-5}	1.6×10^{-3}	0.001	0.1	1	0.004
RR	2.315	4.126×10^{-4}	0.034	6.42×10^{-5}	0.79	1.60	0.007	0.61	7	0.04	1	0.01	0.85	−1.71	2.08	1.38×10^{-4}	2.9×10^{-5}	0.008	0.1	1	0.004
FR	2.574	4.057×10^{-4}	0.033	6.37×10^{-5}	0.79	1.60	0.007	0.61	7	0.04	1	0.01	0.85	−1.71	2.08	1.35×10^{-4}	2.5×10^{-5}	0.01	0.1	1	0.004

4.1.2. RHT theoretical model. Based on the HJC model, Riedel *et al* proposed the RHT model [87] and made several improvements [92, 93]. The model is used for concrete materials. The elastic limit surface equation, failure limit surface equation and residual strength limit surface equation related to pressure are embedded in the model to describe the evolution laws of the initial yield strength, peak yield strength, and post-peak residual strengths of rock mass materials, respectively [94]. RHT is divided into three stages: the linear elastic phase, the linear strengthening phase, and the damage softening phase. The linear strengthening phase is an advantage of the RHT model, which is characterized by the $P-\alpha$ state equation of porous materials; it highlights the strain-hardening effect of coal and rock media [95]. In contrast, the polynomial state equation of the dense material is used to describe the damage softening stage [96].

The RHT model exists in MAT No.272 material of LS-DYNA and contains 34 parameters. These parameters are summarized as relevant material mechanics parameters, material basic strength parameters, failure limit surface parameters, elastic limit surface parameters, linear strength segment parameters, residual strength limit surface parameters, damage evolution parameters, damage softening effect parameters, etc. Notably, the RHT model was developed as an enhancement to the Johnson and Holmquist (JH) concrete model [97]. Although the AUTODYN model has been widely applied to simulate the damage evolution process in concrete, it is rarely used to model coal and rock materials. In addition, the RHT model has not been widely employed in LS-DYNA [98]. To apply the RHT model in LS-DYNA to simulate the damage evolution processes of coal and rock, the mechanical parameters must be determined based on existing mechanical tests [99–101]. For some parameters that cannot be established temporarily, we refer to the default values in relevant manuals [102]. The results are shown in table 4 (unit: g-cm-us system).

4.2. Simulation results and discussion

With reference to the SHPB test system (figure 3), the simulation model is selected according to the dimensions of the test, as shown in figure 14. The lengths of the incident bar and transmission bar are 3000 mm and 2500 mm, respectively, and their diameters are both 50 mm. The material is 35CrMn steel with a density of 7800 kg m^{-3} and an elastic modulus of 206 GPa. In the model, a solid 164 eight-node hexahedron element is selected for grid generation. The axial directions of the bullet, incident bar, sample and transmission bar are divided into 44, 375, 50, and 312 parts, respectively. SET_SEGMENT is defined at the rear end face of the transmission bar to set the boundary condition. The contact type between the bullet and bar is set to ERODING_SURFACE_TO_SURFACE, and the contact type between the bar and the test piece is set to AUTOMATIC_SURFACE_To_ SURFACE, ignoring friction between contact surfaces. A penalty function is set to reduce the hourglass effect in the contact algorithm. The HJC and RHT constitutive models are selected to simulate the failure processes of coal and rock specimens under SHPB impact, and the simulation results are compared with the experimental results.

To verify the accuracy of the simulation results, it is necessary to compare the dynamic response characteristics obtained based on the HJC and RHT constitutive models with the experimental results. Due to space limitations, we take the time-stress curves at the impact velocity level of 6 m s^{-1} as an example. The data collected in the experiment is shown in figure 6(b). On this basis, the incident wave, reflected wave and transmission wave curves obtained by simulation are added. The results are shown in figure 15. The figure shows that whether based on the HJC or RHT constitutive model, the simulation results are similar to the measured results, which shows that it is feasible to use LS-DYNA software to conduct SHPB simulation of coal and rock materials; the selected constitutive model accurately reflects the dynamic response characteristics of coal and rock masses under impact conditions. Specifically, the measured curves of the incident-reflected stress waves of each coal and rock sample are in good agreement with the simulated curve. At the peak value of the incident waves, the measured results are similar to the simulation results. Correspondingly, the measured peak values of reflected waves are significantly lower than the simulated values, which is obviously caused by the energy attenuation and loss of stress waves during propagation. In addition, due to the heterogeneity of coal and rock materials, the measured curves of transmission waves are often slightly more complex than the simulated curves, and their value has certain volatility. Overall, the measured value and the simulated value of the stress wave are slightly different by the same order of magnitude, and the simulation results are reasonable.

According to the consistency comparison of stress waveforms, we verify the accuracy of the LS-DYNA simulation results. Moreover, the damage process of the specimen is reproduced by numerical simulations. By taking the roof rock sample (RR1) as an example, the experimental and simulation comparison diagram of the specimen failure process is shown in figure 16(a). The impact velocity of the bullet is 4.377 m s^{-1}. The bullet takes 29 ms from the contact between the incident bar and the sample to the ejection of rock fragments. A total of eight test pictures are captured every 4 ms. The HJC and RHT constitutive models are used to describe the failure rule of the specimen under SHPB impact; the front view of the simulation results is intercepted, in which the interception time and angle are consistent with the experiment. The experimental diagrams show that when the sample is impacted, the microcracks are derived from the middle of the sample and extend along the axial direction to the contact between the two ends of the sample and the bar, finally forming several splitting cracks that run throughout the sample. With time, the cracks gradually expand and develop from the surface to the interior. Furthermore, several cracks are connected with each other, which makes the crack distribution on the surface of the sample more complex. Relative to the experimental results, the simulations based on the HJC and RHT constitutive models show similar crack evolution laws. Fracture first occurs in the middle of the specimen, then the cracks develop along the axial direction to the end face, and finally,

Table 4. Determination of RHT constitutive model parameters.

Parameters symbols	Description of parameters	Value C/RR/FR	Parameters symbols	Description of parameters	Value C/RR/FR
ρ_0	Material density	1.227/2.315/2.574	D_2	Damage parameters	1/1/1
f_c	Uniaxial compressive strength	1.857×10^{-4}/4.126×10^{-4}/4.057×10^{-4}	P_{comp}	Pressure during pore compaction	0.60/0.55/0.50
α_0	Initial porosity	8.67/1.41/1.53	N	Porosity index	3.0/5.8/4.0
${f_t}^*$	Tensile-to-compressive strength ratio	0.1/0.1/0.1	${f_s}^*$	Shear-to-compressive strength ratio	0.18/0.45/0.38
G	Shear modulus	0.016/0.034/0.033	${g_c}^*$	Compression yield surface parameters	0.53/0.30/0.40
P_{el}	Pressure at pore compression	6.19×10^{-5}/1.38×10^{-4}/1.35×10^{-4}	${g_t}^*$	Tensile yield surface parameters	0.7/0.7/0.7
A_1	Hugonew factor	0.763/0.158/0.867	ξ	Shear modulus reduction factor	0.5/0.5/0.5
A_2	Hugonew factor	0.4577/0.2661/1.4567	A	Failure surface parameters	1.6/1.6/1.6
A_3	Hugonew factor	0.0915/0.1626/0.8903	n	Failure surface index	0.61/0.56/0.56
B_0	Equation of state parameters	0.60/1.68/1.68	Q_0	Tensile meridian ratio	0.68/0.54/0.64
B_1	Equation of state parameters	0.60/1.68/1.68	B	Bare angle correlation coefficient	0.0105/0.0105/0.0105
T_1	Equation of state parameters	0.7629/0.1584/0.8674	β_c	Compressive strain rate index	0.199/0.199/0.199
T_2	Equation of state parameters	0/0/0	β_t	Tensile strain rate index	0.0099/0.0099/0.0099
${\dot{\varepsilon}_0}^c$	Failure compression strain rate	3×10^{-11}/3×10^{-11}/3×10^{-11}	D_1	Initial damage parameters	0.04/0.053/0.042
${\dot{\varepsilon}_0}^t$	Failure compression strain rate	3×10^{-12}/3×10^{-12}/3×10^{-12}	${\varepsilon_0}^m$	Minimum failure strain	2/2/2
${\varepsilon_0}^c$	Failure compression strain rate	3×10^{19}/3×10^{19}/3×10^{19}	A_f	Residual stress strength parameter	1.60/1.63/1.60
${\varepsilon_0}^t$	Reference tensile strain rate	3×10^{19}/3×10^{19}/3×10^{19}	n_f	Residual stress strength index	0.61/0.59/0.56

multiple cracks are connected along the circumferential direction. The simulation results are basically similar to the experimental results, thus verifying the accuracy of the simulation results. Notably, in the numerical simulation, the failure causes of the surface and internal microelements of the specimen are different. The surface microelement is basically in the compression state. There is a natural free surface on one end face, and its failure reason is mainly excessive strain. In contrast, the internal microelement is restrained by the peripheral microelements due to their deformation; thus, the strain is not large and they are prone to local tension. A few microelements are destroyed first because the tensile stress reaches the limit value. When an internal microelement is damaged, the surrounding microelements form a free surface due to the constraint disappearance, leading to the consequences of strain increase and final failure, forming a damage accumulation phenomenon at the crack tip.

Figures 16(b)–(d) show a comparison of the research results of different impact speeds and samples. The crack evolution law is indeed affected by both the impact energy and the physical properties of the test piece. This point has been fully explained previously and is not repeated here. In the LS-DYNA simulation, with increasing impact velocity, the numbers of damaged microelements increase significantly, the sizes of microelements decrease correspondingly, and the damage degrees of the samples increase accordingly.

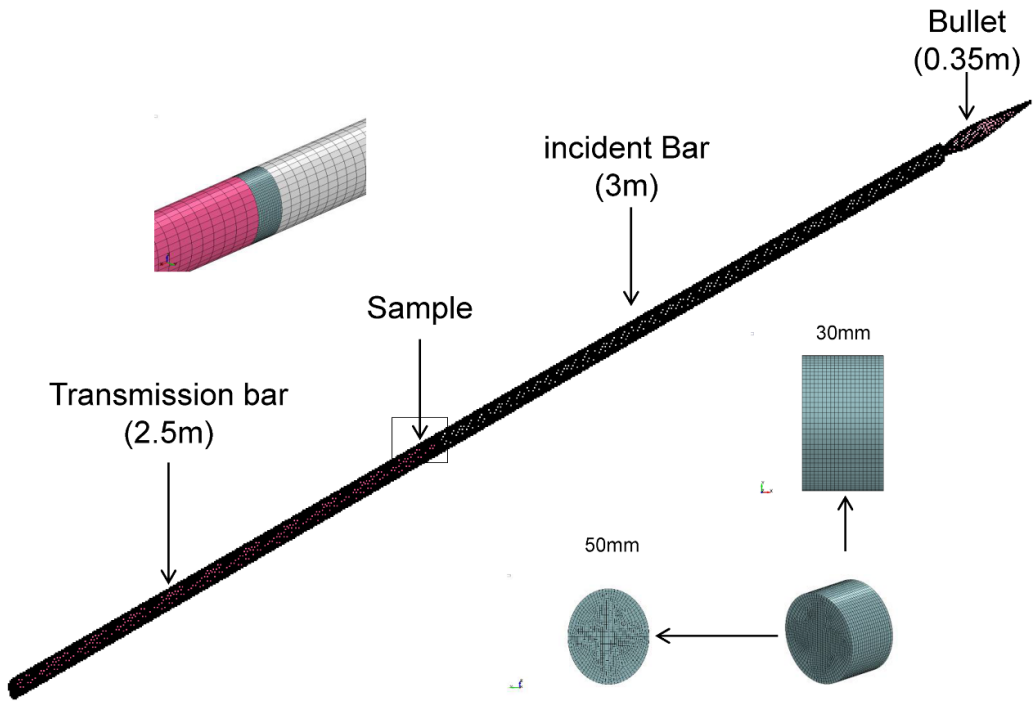

Figure 14. Model establishment and grid division.

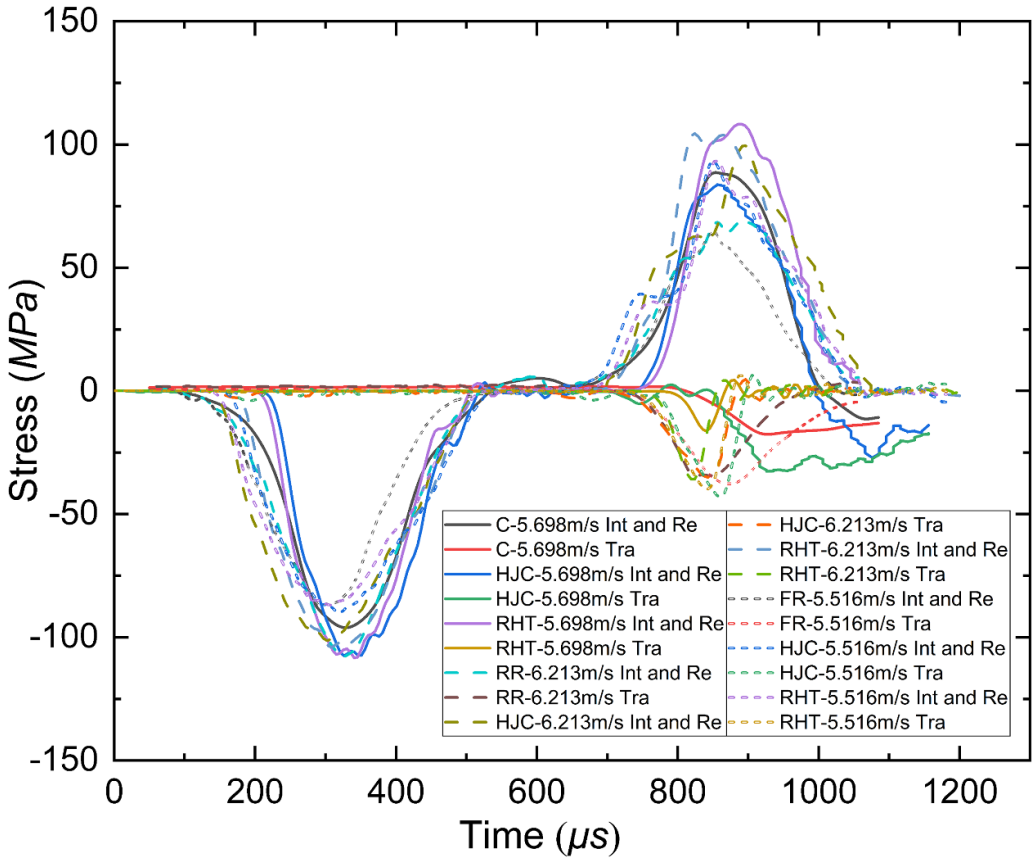

Figure 15. Comparison of stress wave-time curves between experimental and simulated results (Int: incident wave, Re: reflected wave, and Tra: transmitted wave).

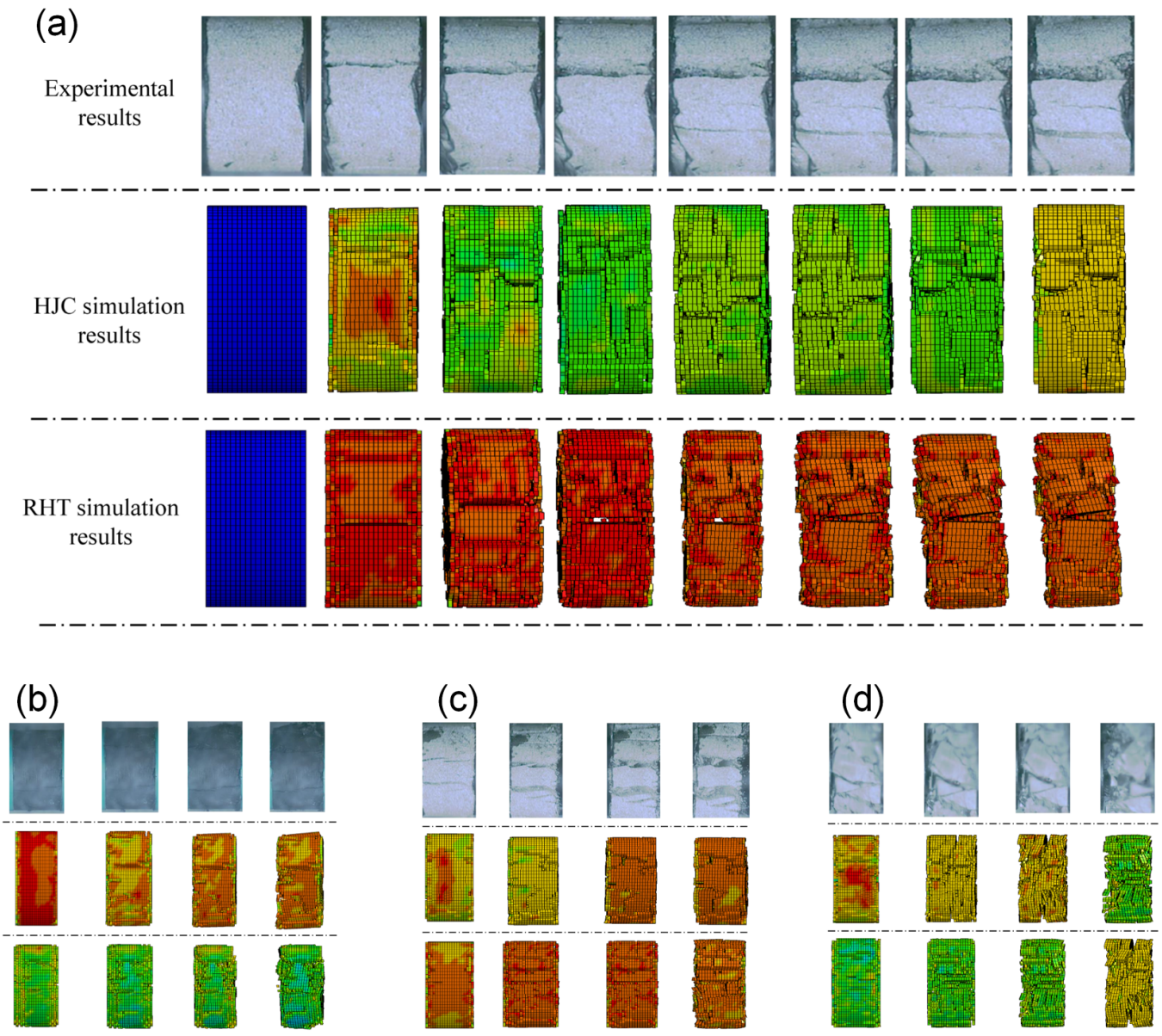

Figure 16. Comparison between experimental and simulated results of coal and rock failure: (a) RR-4.377 m s^{-1}; (b) C-5.698 m s^{-1}; (c) RR-9.213 m s^{-1}; and (d) FR-11.865 m s^{-1}.

Furthermore, the number of points involved in the initial failure increases, and the disorder of crack propagation further increases. The failure form of coal and rock changes from 'crack gradually penetrated' to 'instant fracturing crushing'. In addition, by comparing the simulation results of HJC and RHT, the latter shows a higher agreement with the experimental results. The reason for this phenomenon is that the RHT is proposed based on the HJC. RHT introduces the third invariant of the deviatoric stress tensor and effectively distinguishes the tension and compression meridians. Relative to HJC, RHT is more sensitive to impact and better describes the mechanical properties and damage characteristics of coal and rock materials under dynamic loading.

Since the coal and rock masses are heterogeneous and opaque anisotropic materials, the initiation and propagation of cracks are three-dimensional, leading to the deviation of surface cracks in the comparison between the experimental and simulation results. In addition, there are typically two ways for simulation of the fracture process and failure prediction of coal and rock materials under dynamic test, i.e. mesh-based simulation methods and mesh-less simulation methods [25]. In this article, LS-DYNA, a mesh-based method, is used to simulate coal and rock impact. When large deformations occur, it is challenging to maintain the nonsingularity and continuity of the mesh. Accordingly, a series of mesh-less simulation methods such as smoothed particle hydrodynamics(SPH) [103–106], cracking particle model (CPM) [107, 108], and reproducing kernel particle method (RKPM) [109, 110] are proposed. Due to the separation of constraints from meshes and elements, mesh-less methods are particularly suitable for studying oversized deformation and crack growth such as impact. In future work,

we attempt to explain the evolution laws of coal and rock fractures from the perspectives of three-dimensional and meshless simulation to improve the comprehensiveness of the conclusions.

5. Conclusions

In this study, coal and rock samples obtained at the same location are taken as the research objects, and the dynamic mechanical properties and crack evolution laws under impact loading are systematically analyzed using indoor experiments and numerical simulation methods. The following conclusions are drawn:

(1) The dynamic mechanical properties of coal and rock are affected by the impact velocity and the physical properties of the medium during SHPB impact. The prepared experimental samples have both consistency and differences. At similar impact velocities, the denser the sample is, the faster the stress wave propagates. Although rock and coal are both elastic−plastic complexes, the former is more inclined to show its brittleness; the latter plasticity and ductility yield is more prominent. With increasing impact velocity, the strain strengthening is gradually obvious, and the brittleness of the sample is more typical.
(2) The surface cracks in the processes of coal and rock impact failure have obvious self-similarity, and the box dimension is applicable to quantitatively describe the crack evolution law. In general, the box dimensions of the coal and rock specimens show the regularity of overall increase and local oscillation, and the degree of oscillation of the rock specimen is more intense than that of the coal specimen. The growth rate of the box dimension is relatively fast at the initial stage; the subsequent increasing trend slows. When the impact velocity is low, the box dimensions of the rock samples are larger than those of the coal samples. When the impact speed is high, the opposite phenomenon is true.
(3) The fragment distributions of coal and rock after impact damage have good fractal laws. There is a good logarithmic correlation between the cumulative mass percentage of the particle size under the sieve and the diameter of the sample sieve. The fractal dimension fluctuates between 1.1601 and 2.6029, and the fitting coefficient is relatively high.
(4) Both the box fractal dimension and mass fractal dimension are quantitative characterizations of the impact failure of the specimen, and there is a certain positive correlation between them and the impact speed. With increasing impact speed, more energy is used for crack propagation and the generation of a new fracture surface, resulting in a synchronous increase in the box fractal dimension and mass fractal dimension. These two dimensions are different expressions of coal and rock failure, and their unification is helpful for comprehensively reflecting the failure processes of coal and rock under impact conditions.
(5) Based on the HJC and RHT constitutive models, LS-DYNA simulates the crack evolution process under impact load. The simulation results are in good agreement with the experimental results. Relative to HJC, the simulation based on the RHT constitutive relation better describes the mechanical and damage characteristics of coal and rock materials under dynamic loading.

Data availability statement

The data cannot be made publicly available upon publication because no suitable repository exists for hosting data in this field of study. The data that support the findings of this study are available upon reasonable request from the authors.

Acknowledgments

This research is supported by Fundamental Research Program of Shanxi Province (202103021224277), Scientific and Technological Innovation Programs of Higher Education Institutions in Shanxi (2021L325, 2021L334). These supports are greatly acknowledged and appreciated.

Conflict of interest

There are no conflicts to declare.

ORCID iDs

Xiaoyuan Sun https://orcid.org/0000-0002-6624-0141
Tingxu Jin https://orcid.org/0000-0002-4814-6936
Jihui Li https://orcid.org/0000-0003-3975-9113
Jianlin Xie https://orcid.org/0000-0001-5741-5811
Chuantian Li https://orcid.org/0000-0002-6227-7131
Xiaoxia Li https://orcid.org/0000-0002-4330-3840

References

[1] Zhu W, Wei J, Niu L, Li S and Li S 2018 Numerical simulation on damage and failure mechanism of rock under combined multiple strain rates *Shock Vib.* **2018** 4534250
[2] He M C, Xie H P, Peng S P and Jiang Y D 2005 Study on rock mechanics in deep mining engineering *Chin. J. Rock Mech. Eng.* **24** 2803–13
[3] Zhu W C, Bai Y, Li X B and Niu L L 2012 Numerical simulation on rock failure under combined static and dynamic loading during SHPB tests *Int. J. Impact Eng.* **49** 142–57
[4] Xie L X, Lu W B, Zhang Q B, Jiang Q H, Wang G H and Zhao J 2016 Damage evolution mechanisms of rock in deep tunnels induced by cut blasting *Tunn. Undergr. Space Tech.* **58** 257–70
[5] Cai C G and Wang Y A 2004 Qualitative and quantitative analysis of general regularity of coal and gas outburst *China Saf. Sci. J.* **14** 109–12
[6] Liang B, Wang B and Li G 2014 On the mechanism of the rock-bursts at the roadway sides induced by the dynamic disturbance *J. Saf. Environ.* **14** 13–18
[7] Zhang Q B and Zhao J 2014 A review of dynamic experimental techniques and mechanical behaviour of rock materials *Mec. Roches* **47** 1411–78

[8] ISRM 1979 Suggested methods for determining the uniaxial compressive strength and deformability of rock materials *Int. J. Rock Mech. Min. Sci. Geomech. Abstr.* **16** 135–40

[9] ISRM 1983 Suggested methods for determining the strength of rock materials in triaxial compression: revised version *Int. J. Rock Mech. Min. Sci. Geomech. Abstr.* **20** 285–90

[10] Li X B, Zhou Z L, Ye Z Y, Ma C D, Zhao F J, Zuo Y J and Hong L 2008 Study of rock mechanical characteristics under coupled static and dynamic loads *Chin. J. Rock Mech. Eng.* **27** 1387–95

[11] Gong F Q, Si X F, Li X B and Wang S Y 2019 Dynamic triaxial compression tests on sandstone at high strain rates and low confining pressures with split Hopkinson pressure bar *Int. J. Rock Mech. Min.* **113** 211–9

[12] Yin T B, Li X B, Gong F Q, Zhou Z L and Gao K 2012 Study of dynamic failure processes and mechanism of rock subjected to coupling temperature and pressure *Chin. J. Rock Mech. Eng.* **31** 2814–20

[13] Chen R, Xia K, Dai F, Lu F and Luo S N 2009 Determination of dynamic fracture parameters using a semi-circular bend technique in split Hopkinson pressure bar testing *Eng. Fract. Mech.* **76** 1268–76

[14] Zhang Z X, Kou S Q, Yu J, Yu Y, Jiang L G and Lindqvist P A 1999 Effects of loading rate on rock fracture *Int. J. Rock Mech. Min.* **36** 597–611

[15] Daniel I M and Rowlands R E 1975 On wave and fracture propagation in rock media *Exp. Mech.* **15** 449–57

[16] Cai M and Liu D 2009 Study of failure mechanisms of rock under compressive-shear loading using real-time laser holography *Int. J. Rock Mech. Min.* **46** 59–68

[17] Yang R S, Yue Z W, Sun Z H, Xiao T S and Guo D M 2009 Dynamic fracture behavior of rock under impact load using the caustics method *Min. Sci. Technol.* **19** 79–83

[18] Chen W W, Hudspeth M C, Claus B, Parab N D, Black J T, Fezzaa K and Luo S N 2015 *In situ* damage assessment using synchrotron x-rays in materials loaded by a Hopkinson bar *Phil. Trans.* A **372** 20130191

[19] Shi W, Wu Y and Wu L 2007 Quantitative analysis of the projectile impact on rock using infrared thermography *Int. J. Impact Eng.* **34** 990–1002

[20] Perkins R D and Green S J 1968 High speed photography in dynamic materials testing *Rev. Sci. Instrum.* **39** 1209–10

[21] Peters W H and Ranson W F 1982 Digital imaging techniques in experimental stress analysis *Opt. Eng.* **21** 427–31

[22] Gao G, Huang S, Xia K and Li Z 2015 Application of digital image correlation (DIC) in dynamic notched semi-circular bend (NSCB) tests *Exp. Mech.* **55** 95–104

[23] Zhang Q B and Zhao J 2013 Determination of mechanical properties and full-field strain measurements of rock material under dynamic loads *Int. J. Rock Mech. Min.* **60** 423–39

[24] Ai D H, Zhao Y C, Wang Q F and Li C W 2019 Experimental and numerical investigation of crack propagation and dynamic properties of rock in SHPB indirect tension test *Int. J. Impact Eng.* **126** 135–46

[25] Ai D H, Zhao Y C, Wang Q F and Li C W 2020 Crack propagation and dynamic properties of coal under SHPB impact loading: experimental investigation and numerical simulation *Theor. Appl. Fract. Mech.* **105** 102393

[26] Germanovich L N, Salganik R L, Dyskin A V and Lee K K 1994 Mechanisms of brittle fracture of rock with pre-existing cracks in compression *Pure Appl. Geophys.* **143** 117–49

[27] Dyskin A V, Sahouryeh E, Jewell R J, Joer H and Ustinov K B 2003 Influence of shape and locations of initial 3D cracks on their growth in uniaxial compression *Eng. Fract. Mech.* **70** 2115–36

[28] Lu Y, Wang L and Elsworth D 2015 Uniaxial strength and failure in sandstone containing a pre-existing 3D surface flaw *Int. J. Fract.* **194** 59–79

[29] Fu J W, Chen K, Zhu W S, Zhang X Z and Li X J 2016 Progressive failure of new modelling material with a single internal crack under biaxial compression and the 3D numerical simulation *Eng. Fract. Mech.* **165** 140–52

[30] Li X B, Zhou T and Li D Y 2017 Dynamic strength and fracturing behavior of single-flawed prismatic marble specimens under impact loading with a split-Hopkinson pressure bar *Rock Mech. Rock Eng.* **50** 29–44

[31] Zhang L, Zhang Z J, Chen Y, Dai B and Wang B 2022 Crack development and damage patterns under combined dynamic-static loading of parallel double fractured rocks based on DIC technique *Acta Geotech.* **18** 877–901

[32] Zhu J B, Zhou T, Liao Z Y, Sun L, Li X B and Chen R 2018 Replication of internal defects and investigation of mechanical and fracture behaviour of rock using 3D printing and 3D numerical methods in combination with x-ray computerized tomography *Int. J. Rock Mech. Min. Sci.* **106** 198–212

[33] Zhou X P, Zhang J Z and Wong L N Y 2018 Experimental study on the growth, coalescence and wrapping behaviors of 3D cross-embedded flaws under uniaxial compression *Rock Mech. Rock Eng.* **51** 1379–400

[34] Zhou T, Zhu J B, Ju Y and Xie H P 2019 Volumetric fracturing behaviour of 3D printed artificial rocks containing single and double 3D internal flaws under static uniaxial compression *Eng. Fract. Mech.* **205** 190–204

[35] Zhou T, Zhu J B and Xie H P 2020 Mechanical and volumetric fracturing behaviour of three-dimensional printing rock-like samples under dynamic loading *Rock Mech. Rock Eng.* **53** 2855–64

[36] Sharafisafa M and Shen L 2020 Experimental investigation of dynamic fracture patterns of 3d printed rock-like material under impact with digital image correlation *Rock Mech. Rock Eng.* **53** 3589–607

[37] Xie H P, Gao F, Zhou H W and Zuo J P 2003 Fractal fracture and fragmentation in rocks *J. Disaster Prev. Mitig. Eng.* **23** 1–9

[38] Li Y, Zhang S and Zhang X 2018 Classification and fractal characteristics of coal rock fragments under uniaxial cyclic loading conditions *Arab. J. Geosci.* **11** 1–12

[39] Ma T R, Ma D P and Yang Y J 2020 Fractal characteristics of coal and sandstone failure under different unloading confining pressure tests *Adv. Mater. Sci. Eng.* **2020** 1–11

[40] Hou T X, Xu Q and Zhou J W 2015 Size distribution, morphology and fractal characteristics of brittle rock fragmentations by the impact loading effect *Acta Mech.* **226** 3623–37

[41] Li C J, Xu Y, Chen P Y, Li H L and Lou P J 2020 Dynamic mechanical properties and fragment fractal characteristics of fractured coal–rock-like combined bodies in split Hopkinson pressure bar tests *Nat. Resour. Res.* **29** 3179–95

[42] Yin P, Ma H C, Liu X W, Bi J, Zhou X P and Berto F 2018 Numerical study on the dynamic fracture behavior of 3D heterogeneous rocks using general particle dynamics *Theor. Appl. Fract. Mech.* **96** 90–104

[43] Li X B, Zou Y and Zhou Z L 2014 Numerical simulation of the rock SHPB test with a special shape striker based on the discrete element method *Rock Mech. Rock Eng.* **47** 1693–709

[44] Li F, Wang C C, Sun R C, Xiang G Y, Ren B R and Zhang Z 2022 Frequency response characteristics and failure model of single-layered thin plate rock mass under dynamic loading *Sci. Rep.* **12** 19047

[45] Kong X G, Li S G, Wang E Y, Wang X, Zhou Y X, Ji P F, Shuang H, Li S and Wei Z 2021 Experimental and

numerical investigations on dynamic mechanical responses and failure process of gas-bearing coal under impact load *Soil Dyn. Earthq. Eng.* **142** 106579
[46] Xu D D, Wu A Q and Li C 2019 A linearly-independent higher-order extended numerical manifold method and its application to multiple crack growth simulation *J. Rock Mech. Geotech.* **11** 1256–63
[47] Wu J Y, Nguyen V P, Nguyen C T, Sutula D, Sinaie S and Bordas S P 2020 Chapter one-phase-field modeling of fracture *Adv. Appl. Mech.* **53** 1–183
[48] Zhang W B, Shen Z Z, Ren J, Gan L, Xu L Q and Sun Y Q 2021 Phase-field simulation of crack propagation in quasi-brittle materials: COMSOL implementation and parameter sensitivity analysis *Model. Simul. Mater. Sci. Eng.* **29** 055020
[49] Wu J Y and Chen W X 2022 On the phase-field modeling of fully coupled chemo-mechanical deterioration and fracture in calcium leached cementitious solids *Int. J. Solids Struct.* **238** 111380
[50] Wang Q R, Song E X, Xu P, He Y S, Shi X Y and Xie H Z 2023 Dynamic performance and stress wave propagation characteristics of parallel jointed rock mass using the SHPB technique *KSCE J. Civ. Eng.* 1–12
[51] Zhou S W and Zhuang X Y 2018 Adaptive phase field simulation of quasi-static crack propagation in rocks *Undergr. Space* **3** 190–205
[52] Zhu H Q, Fang S H, Zhang Y L and Wu Y 2020 Study on the dynamic response characteristics of cylindrical coal-rock samples under dynamic loads *Shock Vib.* 1–12
[53] P Y L, Hu B, G L X, Yang Z Z and Yu L 2020 Calculation model of hydraulic crack vertical propagation in coal-sand interbedded formation based on the phase field method *China Coal Soc.* 706–16
[54] Li X J, Zhang Y Y, Shi C and Chen X D 2020 Experimental and numerical study on tensile strength and failure pattern of high performance steel fiber reinforced concrete under dynamic splitting tension *Constr. Build. Mater.* **259** 119796
[55] Zhang W B, Shi D D, Shen Z Z, Wang X H, Gan L, Shao W, Tang P, Zhang H W and Yu S Y 2023 Effect of calcium leaching on the fracture properties of concrete *Constr. Build. Mater.* **365** 130018
[56] Zhang W B, Shi D D, Shen Z Z, Shao W, Gan L, Yuan Y, Tang P, Zhao S and Chen Y S 2023 Reduction of the calcium leaching effect on the physical and mechanical properties of concrete by adding chopped basalt fibers *Constr. Build. Mater.* **365** 130080
[57] Xu J Y, Fan J S and Lu X C 2012 *Dynamic Mechanical Properties of Rock with the Confining Pressure* (Xian: Northwestern Polytechnical University Press)
[58] Tan Y Y, Yu X, Elmo D, Xu L H and Song W D 2019 Experimental study on dynamic mechanical property of cemented tailings backfill under SHPB impact loading *Int. J. Miner. Metall. Mater.* **26** 404–16
[59] Yuan Q, Wang L, Xie G, Gu S, Khan N M, Jiao Z and Liu H 2022 Evaluation of the energy consumption and fractal characteristics of different length-diameter ratios of coal under dynamic impact *Energies* **15** 5498
[60] Wang L, Yuan Q, Xie G, Gu S, Jiao Z, Liu H and Chen L 2022 Length-diameter ratio effect of energy dissipation and fractals of coal samples under impact loading *China Coal Soc.* **47** 1534–46
[61] Zhou Y X, Xia K W, Li X B, Li H B, Ma G W, Zhao J and Dai F 2011 Suggested methods for determining the dynamic strength parameters and mode-I fracture toughness of rock materials *Int. J. Rock Mech. Min.* **49** 105–12
[62] Zhao H and Gary G 1996 On the use of SHPB techniques to determine the dynamic behavior of materials in the range of small strains *Int. J. Solids Struct.* **33** 3363–75
[63] Xie H P, Wang J A and Kwaśniewski M A 1999 Multifractal characterization of rock fracture surfaces *Int. J. Rock Mech. Min.* **36** 19–27
[64] Grasselli G, Wirth J and Egger P 2002 Quantitative three-dimensional description of a rough surface and parameter evolution with shearing *Int. J. Rock Mech. Min.* **39** 789–800
[65] Grasselli G and Egger P 2003 Constitutive law for the shear strength of rock joints based on three-dimensional surface parameters *Int. J. Rock Mech. Min.* **40** 25–40
[66] Ding C X, Yang R S and Yang L Y 2021 Experimental results of blast-induced cracking fractal characteristics and propagation behavior in deep rock mass *Int. J. Rock Mech. Min.* **142** 104772
[67] Nayak S R, Mishra J and Palai G 2019 Analysing roughness of surface through fractal dimension: a review *Image Vis. Comput.* **89** 21–34
[68] Ai T, Zhang R, Zhou H W and Pei J L 2014 Box-counting methods to directly estimate the fractal dimension of a rock surface *Appl. Surf. Sci.* **314** 610–21
[69] Liu C, Zhan Y, Deng Q S, Qiu Y J and Zhang A 2021 An improved differential box counting method to measure fractal dimensions for pavement surface skid resistance evaluation *Measurement* **178** 109376
[70] Falconer K 2004 *Fractal Geometry: Mathematical Foundations and Applications* (New York: Wiley)
[71] Iakovidis D K, Goudas T, Smailis C and Maglogiannis I 2014 Ratsnake: a versatile image annotation tool with application to computer-aided diagnosis *Sci. World J.* **2014** 286856
[72] Li M, Zhang J X, Guo Y M, Pu H and Peng Y F 2022 Influence of particle size distribution on fractal characteristics of waste rock backfill materials under compression *J. Mater. Res. Technol.* **20** 2977–89
[73] Wang J G, Zuo T, Li X L, Tao Z H and Ma J 2021 Study on the fractal characteristics of the pomegranate biotite schist under impact loading *Geofluids* 1570160
[74] Mandelbrot B B 1985 Self-affine fractals and fractal dimension *Phys. Scr.* **32** 257
[75] Zhao L P, Cao Y X, Lyu S F, Li J Y and Tian L 2022 Coal structure characteristics in the northern Qinshui basin and their discrimination method based on the particle size of drilling cuttings *ACS Omega* **7** 22956–68
[76] Sun X, Chen Y, G Y, Li J, Xu H, X M, Fu S, Xie J and Liang L 2020 Propagation characteristics of ultrasonic P-wave velocity in artificial jointed coal briquettes *J. Geophys. Eng.* **17** 827–37
[77] ASTM 2008 D2845-08 Test method for laboratory determination of pulse velocities and ultrasonic elastic constants of rock *Annual Book of ASTM Standards* (West Conshohocken: ASTM International)
[78] Li X B, Lok T S, Zhao J and Zhao P J 2000 Oscillation elimination in the Hopkinson bar apparatus and resultant complete dynamic stress-strain curves for rocks *Int. J. Rock Mech. Min.* **37** 1055–60
[79] Kizhner S, Flatley T P, Huang N E, Blank K and Conwell E 2004 On the Hilbert-Huang transform data processing system development *Proc. 2004 IEEE Aerospace Conf. Proc. (IEEE Cat. No.04TH8720)* (*Big Sky, MT, USA, 6–13 March 2004*) pp 1961–78
[80] Xie B J, Wang X Y and Lu P Y 2017 Dynamic properties of bedding coal and rock and the SHPB testing for its impact damage *J. Vib. Shock* **36** 117–24
[81] Wu N, Fu J Y and Xiong C 2022 Studying the characteristics of chaos and fractals of construction rocks under different loading velocities *Materials* **15** 7890

[82] Sun X Y, Li J H, Ding H, Jin T X, Xie J L and Liang L 2022 Experimental study on the impact damage characteristics of coal-rock based on SHPB dynamic loading process *Coal Chem.* **45** 1–5
[83] ASTM 2016 E11-16 Standard specification for woven wire test sieve cloth and test sieves *Annual Book of ASTM Standards* (West Conshohocken: ASTM International)
[84] Wang Y X, Lin H, Zhao Y L, Li X, Guo P P and Liu Y 2019 Analysis of fracturing characteristics of unconfined rock plate under edge-on impact loading *Eur. J. Environ. Civ. Eng.* **24** 1–16
[85] Abedini M and Zhang C W 2021 Performance assessment of concrete and steel material models in ls-dyna for enhanced numerical simulation, a state of the art review *Arch. Comput. Methods Eng.* **28** 2921–42
[86] Holmquist T J, Johnson G R and Cook W H 1993 A computational constitutive model for concrete subjected to large strains, high strain rates, and high pressures *Proc. 14th Int. Symp. on Ballistics* (*Quebec*) pp 591–600
[87] Riedel W, Thoma K, Hiermaier S and Schmolinske E 1999 Penetration of reinforced concrete by BETA-B-500 numerical analysis using a new macroscopic concrete model for hydrocodes *Proc. 9th Int. Symp. on the Effects of Munitions with Structures* (*Berlin*) pp 315–22
[88] Xie B J, Yan Z, Du Y J, Zhao Z M and Zhang X Q 2019 Determination of Holmquist-Johnson-Cook constitutive parameters of coal: laboratory study and numerical simulation *Processes* **7** 386
[89] Xie B J, Chen D X, Ding H, Wang G Y and Yan Z 2020 Numerical simulation of Split-Hopkinson pressure bar tests for the combined coal-rock by using the Holmquist–Johnson–Cook model and case analysis of outburst *Adv. Civ. Eng.* **2020** 8833233
[90] Wang Z L, Wang H C, Wang J G and Tian N C 2021 Finite element analyses of constitutive models performance in the simulation of blast-induced rock cracks *Comput. Geotech.* **135** 104172
[91] Bhat I, Rupali S and Kumar A 2022 Experimental and numerical analysis of constitutive characteristics in bituminous coal *Sādhanā* **47** 159
[92] Riedel W 2000 *Beton Unter Dynamischen Lasten: Meso-und Makromechanische Modelle Und Ihre Parameter* (London: EMI)
[93] Riedel W, Kawai N and Kondo K-I 2009 Numerical assessment for impact strength measurements in concrete materials *Int. J. Impact Eng.* **36** 283–93
[94] Chen W F 1982 *Plasticity in Reinforced Concrete* (New York: McGraw Hill)
[95] Herrmann W 1969 Constitutive equation for the dynamic compaction of ductile porous material *J. Appl. Phys.* **40** 2490–9
[96] Autodyn 1999 *Autodyn Theory Manual* (Horsham: Century Dynamics Ltd)
[97] Tu Z G and Lu Y 2009 Evaluation of typical concrete material models used in hydrocodes for high dynamic response simulations *Int. J. Impact Eng.* **36** 132–46
[98] Xie L X, Lu W B, Zhang Q B, Jiang Q H, Chen M and Zhao J 2017 Analysis of damage mechanisms and optimization of cut blasting design under high *in-situ* stresses *Tunn. Undergr. Space Technol.* **66** 19–33
[99] Banadaki M D and Mohanty B 2012 Numerical simulation of stress wave induced fractures in rock *Int. J. Impact Eng.* **40** 16–25
[100] Xie L X, Yang S Q, Gu J C, Zhang Q B, Lu W B, Jing H W and Wang Z L 2019 JHR constitutive model for rock under dynamic loads *Comput. Geotech.* **108** 161–72
[101] Yang X L, Wang C, Chu H B, Yan S Y, Wei H X and Yu M F 2022 Study on the stress field and crack propagation of coal mass induced by high-pressure air blasting *Minerals* **12** 300
[102] Borrvall T and Riedel W 2011 The RHT concrete model in LS-DYNA *Proc. 8th European LS-DYNA User Conf.* (*Strasbourg, France*)
[103] Lucy L B 1977 A numerical approach to the testing of the fission hypothesis *Astron. J.* **82** 1013–24
[104] Libersky L D, Petschek A G, Carney T C, Hipp J R and Allahdadi F A 1993 High strain Lagrangian hydrodynamics: a three-dimensional SPH code for dynamic material response *J. Comput. Phys.* **109** 67–75
[105] Yu S Y, Yu J, Sun Z H, Zhu C H and Yang J 2023 Numerical investigation and experimental study on fracture processes of central flawed sandstone Brazilian discs *Int. J. Solids Struct.* **262** 112054
[106] Yu S Y, Sun Z H, Qian W P, Yu J and Yang J 2023 A meshless method for modeling the microscopic drying shrinkage cracking processes of concrete and its applications *Eng. Fract. Mech.* **277** 109014
[107] Liu W K, Jun S and Zhang Y F 1995 Reproducing kernel particle methods *Int. J. Numer. Methods Fluids* **20** 1081–106
[108] Peng P P, Fu Y D and Cheng Y M 2021 A hybrid reproducing kernel particle method for three-dimensional advection-diffusion problems *Int. J. Appl. Mech.* **13** 2150085
[109] Remmers J J, Borst R D and Needleman A 2003 A cohesive segments method for the simulation of crack growth *Comput. Mech.* **31** 69–77
[110] Rabczuk T, Zi G, Bordas S and Nguyen-Xuan H 2010 A simple and robust three-dimensional cracking-particle method without enrichment *Comput. Methods Appl. Mech. Eng.* **199** 2437–55